Draft version July 23, 2012
Preprint typeset using LaTeX style emulateapj v. 11/10/09

arXiv:1207.4789v1 [astro-ph.SR] 19 Jul 2012

A *HUBBLE SPACE TELESCOPE* SURVEY OF H_2 EMISSION IN THE CIRCUMSTELLAR ENVIRONMENTS OF YOUNG STARS*

Kevin France[1], Eric Schindhelm[1,2], Gregory J. Herczeg[3,4] Alexander Brown[1], Hervé Abgrall[5], Richard D. Alexander[6], Edwin A. Bergin[7], Joanna M. Brown[8], Jeffrey L. Linsky[9], Evelyne Roueff[5], and Hao Yang[10]

Draft version July 23, 2012

ABSTRACT

The formation timescale and final architecture of exoplanetary systems are closely related to the properties of the molecular disks from which they form. Observations of the spatial distribution and lifetime of the molecular gas at planet-forming radii ($a < 10$ AU) are important for understanding the formation and evolution of exoplanetary systems. Towards this end, we present the largest spectrally resolved survey of H_2 emission around low-mass pre-main sequence stars compiled to date. We use a combination of new and archival far-ultraviolet spectra from the COS and STIS instruments on the *Hubble Space Telescope* to sample 34 T Tauri stars (27 actively accreting CTTSs and 7 non-accreting WTTSs) with ages ranging from $\sim 1 - 10$ Myr. We observe fluorescent H_2 emission, excited by Lyα photons, in 100% of the accreting sources, including all of the transitional disks in our sample (CS Cha, DM Tau, GM Aur, UX Tau A, LkCa15, HD 135344B and TW Hya). The spatial distribution of the emitting gas is inferred from spectrally resolved H_2 line profiles. Some of the emitting gas is produced in outflowing material, but the majority of H_2 emission appears to originate in a rotating disk. For the disk-dominated targets, the H_2 emission originates predominately at $a \lesssim 3$ AU. The emission line-widths and inner molecular radii are found to be roughly consistent with those measured from mid-IR CO spectra.

Subject headings: protoplanetary disks — stars: pre-main sequence — ultraviolet: planetary systems

1. INTRODUCTION

The lifetime, spatial distribution, and composition of gas and dust in the inner ~ 10 AU of young (age $\lesssim 10$ Myr) circumstellar disks are important components for understanding of the formation and evolution of extrasolar planetary systems. The formation of giant planet cores and their accretion of gaseous envelopes occurs on timescales similar to the lifetimes of the disks around Classical T Tauri Stars (CTTSs; $10^6 - 10^7$ yr). The cores of giant planets are thought to be comprised of coagulations of dust grains (Hayashi et al. 1985), and the majority of observational work on the lifetime of inner disks has come from photometric and spectroscopic studies of their dust (Haisch et al. 2001; Hernández et al. 2007; Wyatt 2008). Dust in protoplanetary disks is observed as mid- and far-IR excess flux produced by warm grains (e.g., Furlan et al. 2006, 2009; Evans et al. 2009; Luhman et al. 2010). The IR spectral energy distributions (SEDs) of protoplanetary disks are sensitive to the radial distribution of dust in the disk; this dependence has led to the discovery of a class of "transitional" systems, whose SEDs indicate that gaps of a few tenths to tens of AU have been opened in their inner disks (Strom et al. 1989; Calvet et al. 2002, 2005; Espaillat et al. 2007; and see the review by Williams & Cieza 2011). The physical process by which the inner disk is cleared is not yet established. Possible mechanisms including photoevaporation (Alexander et al. 2006; Gorti et al. 2009) and dynamical clearing by exoplanetary systems (Rice et al. 2003; Dodson-Robinson & Salyk 2011), possibly aided by the magnetorotational instability (Chiang & Murray-Clay 2007), can reproduce certain transitional disk observations.

The lifetime and spatial extent of the gas disk determine the final mass of giant planets (Ida & Lin 2004) and the final architecture of an exoplanetary system, as disk gas regulates type-II planetary migration (Ward 1997; Armitage et al. 2002; Trilling et al. 2002). Because the migration timescale is sensitive to the specifics of the disk surface density distribution and dissipation timescale (Armitage 2007), observations of gas-rich systems with age ≤ 10 Myr can provide important constraints on models of the evolution of exoplanetary systems. Significant observational effort has been devoted to the study of inner disk gas in recent years, including ground-based mid-IR spectroscopy of CO and [Ne II] (Najita et al. 2003;

---

* Based on observations made with the NASA/ESA *Hubble Space Telescope*, obtained from the data archive at the Space Telescope Science Institute. STScI is operated by the Association of Universities for Research in Astronomy, Inc. under NASA contract NAS 5-26555.

[1] Center for Astrophysics and Space Astronomy, University of Colorado, 389 UCB, Boulder, CO 80309, USA; kevin.france@colorado.edu
[2] Current Addesss: Southwest Research Institute, 1050 Walnut Street, Suite 300, Boulder, CO 80302, USA
[3] Max-Planck-Institut für extraterrestriche Physik, Postfach 1312, 85741 Garching, Germany
[4] Current Addesss: Kavli Institute for Astronomy and Astrophysics, Peking University, Beijing 100871, China
[5] LUTH and UMR 8102 du CNRS, Observatoire de Paris, Section de Meudon, Place J. Janssen, 92195 Meudon, France
[6] Department of Physics & Astronomy, University of Leicester, Leicester, LE1 7RH, UK
[7] Department of Astronomy, University of Michigan, 830 Dennison Building, 500 Church Street, Ann Arbor, MI 48109, USA
[8] Harvard-Smithsonian Center for Astrophysics, 60 Garden Street, MS-78, Cambridge, MA 02138, USA
[9] JILA, University of Colorado and NIST, 440 UCB, Boulder, CO 80309
[10] Institute of Astrophysics, Central China Normal University, Wuhan, Hubei, 430079, China

Pascucci et al. 2007; Herczeg et al. 2007; Najita et al. 2009; Bast et al. 2011; Sacco et al. 2012), spectroastrometric observations of CO (Pontoppidan et al. 2008a, 2011) and [Ne II] (Pascucci et al. 2011), and *Spitzer*-IRS observations of H_2O and organics (Carr & Najita 2008; Salyk et al. 2008, 2011b; Carr & Najita 2011). There is growing evidence that remnant gas disk survival is common inside the dust hole in transitional disks (e.g., Salyk et al. 2009, 2011), suggesting that planetary migration may continue after the dust disk has dispersed. In transitional systems with minimal inner disk dust, observations of active accretion also provide indirect evidence for the presence of a remnant gas disk (Najita et al. 2007; Kim et al. 2009; Merín et al. 2010; Fedele et al. 2010).

Many previous studies of inner disk gas have used trace species to infer the presence of molecular hydrogen (H_2), the primary constituent of protoplanetary disks and gas giant planets. The homonuclear nature of H_2 means that rovibrational transitions are dipole forbidden, with weak quadrupole transitions that have large energy spacings. This makes direct detection of H_2 challenging at near- and mid-IR wavelengths (Pascucci et al. 2006; Carmona et al. 2008; but see also Bary et al. 2008). However, H_2 can be observed in the far-UV (912 – 1650 Å) bandpass, where the strong dipole-allowed electronic transition spectrum is primarily photo-excited ("pumped") by stellar Lyα photons (Ardila et al. 2002; Herczeg et al. 2002). The Lyα-pumping route proceeds primarily by absorption out of the second excited vibrational level ($v = 2$) of H_2 (Shull 1978), which implies that the molecules reside in a hot ($T(H_2) > 2000$ K) disk surface at semi-major axes $a < 10$ AU (Herczeg et al. 2004), or in extended outflows (Walter et al. 2003; Saucedo et al. 2003). An analysis of the spectral line profiles can distinguish between these origins, enabling one to identify and characterize emission from the molecular disk given sufficient spectral resolution and spectroscopic sensitivity. Assuming that disk molecules are in Keplerian orbit around their central star, line broadening due to orbital motion dominates the profile in moderate-to-high inclination systems. H_2 velocity widths can therefore be used to infer the spatial distribution of the gas on the disk surface.

In this work, we present the most sensitive survey of spectrally resolved H_2 emission in protoplanetary disks obtained to date. Previous spectral surveys of TTSs with the *International Ultraviolet Explorer* (Valenti et al. 2000; Johns-Krull et al. 2000) and the various ultraviolet spectrographs on *HST* (Ardila et al. 2002; Herczeg et al. 2006; Ingleby et al. 2009; Yang et al. 2012) have been carried out at either lower spectroscopic sensitivity or resolution. In this study, we take advantage of the high sensitivity, low instrumental background, and moderate spectral resolution of the *Hubble Space Telescope*-Cosmic Origins Spectrograph to greatly expand the number of targets available for detailed UV studies. In §2, we describe the targets and the *HST* observations. The analysis performed to characterize the H_2 luminosities and spatial distributions are described in §3. We present in §4 a discussion of H_2 line profiles, considering outflow and disk origins for the emitting gas, and an estimate of the fraction of stellar Lyα re-processed by circumstellar H_2. §4 also presents the time-evolution of the amount and location of the H_2 gas, suggesting that the H_2-emitting gas both dissipates and moves towards larger orbital radii over the interval from $10^6 - 10^7$ yr. A brief summary of the results from the molecular survey are presented in §5.

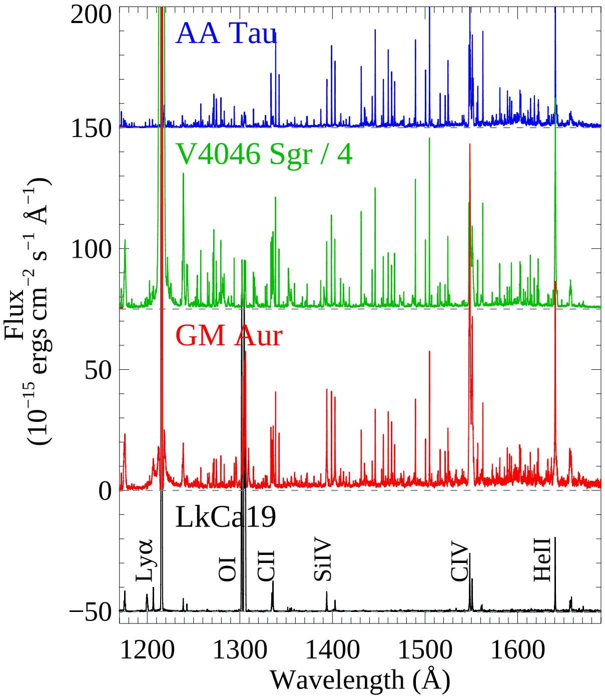

Fig. 1.— Examples of COS spectra (1170 – 1690 Å) for a range of gas and dust disk parameters. From top to bottom: The primordial disk target AA Tau [offset by +150 ($\times 10^{-15}$ erg cm^{-2} s^{-1} Å^{-1})], the pre-transitional disk V4046 Sgr [flux divided by 4 and offset by +75 ($\times 10^{-15}$ erg cm^{-2} s^{-1} Å^{-1})], the transitional disk system GM Aur, and the gas-poor WTTS LkCa19 [offset by -50 ($\times 10^{-15}$ erg cm^{-2} s^{-1} Å^{-1})]. The spectra have been binned by one spectral resolution element (7 pixels) for display. Except for the atomic lines identified in the spectrum of LkCa19, most of the emission lines in the spectra of the other three stars are fluorescent H_2 emission lines pumped by Lyα.

2. TARGET SAMPLE AND OBSERVATIONS

2.1. *Target Sample*

The goal of this observational survey is to span a range of ages, mass accretion rates, and star-forming environments in order to better understand the global properties of H_2 emission in protoplanetary environments. The targets mainly belong to the Taurus-Auriga, η Chamaeleontis, TW Hya, and Chamaeleon I star-forming regions, as well as individual targets in other associations and isolated systems. Potential sources of uncertainty in analyzing a diverse population of targets are systematic effects based on different methods used to derive system parameters in the literature. In order to mitigate the effects of systematics on this study of molecular disks, our approach was to adopt system parameters from papers where similar techniques were used to derive properties such as ages, extinctions, stellar masses, and inclinations. The adopted target parameters are given in Table 1. Where possible, 1) inclinations were taken

TABLE 1
HST Target List

Target[a]	A$_V$	log$_{10}$(Age) (yrs)	M$_*$ (M$_\odot$)	$\dot{M}$ (10^{-8} M$_\odot$ yr^{-1})	i ($\circ$)	HST[a] PID	Ref.[c]
AA Tau	0.50	6.38 ± 0.20	0.80	0.33	75	11616	2,15,28
AK Sco	0.5	7.24 ± 0.24	1.35	0.09	68	11616−*S*	3,24
BP Tau	0.50	5.94 ± 0.29	0.73	2.88	30	12036	1,15,30
CS Cha	0.8	6.39 ± 0.09	1.05	1.20	60	11616	4,25
CV Cha	1.67	6.70 ± 0.10	2.00	3.16	35	11616−*S*	5,26
DE Tau	0.60	5.82 ± 0.20	0.59	2.64	35	11616	1,15,29
DF Tau A	0.60	6.27 ± 0.53	0.19	17.7	85	11533	15,29
DK Tau A	0.80	6.17 ± 0.22	0.71	3.79	50	11616	1,15,29
DM Tau	0.0	6.56 ± 0.20	0.50	0.29	35	11616	2,16,21
DN Tau	1.90	6.04 ± 0.20	0.60	0.35	28	11616	2,15,21,31
DR Tau	3.20	6.18 ± 0.20	0.80	3.16	72	11616	2,17,28
GM Aur	0.10	6.86 ± 0.20	1.20	0.96	55	11616	2,15,21
HD 104237	0.70	6.30 ± 0.30	2.50	3.50	18	11616−*S*	7,19,40
HD 135344B	0.30	6.90 ± 0.30	1.60	0.54	14	11828	8,19,36
HN Tau A	0.5	6.27 ± 0.27	0.85	0.13	>40	11616	1,15,22
IP Tau	0.20	6.37 ± 0.24	0.68	0.08	60	11616	1,15,32
LkCa 15	0.60	6.35 ± 0.26	0.85	0.13	49	11616	1,16,21
RECX 11	0.0	6.60 ± 0.20	0.80	0.03	70	11616	9,20,45
RECX 15	0.0	6.78 ± 0.08	0.40	0.10	60	11616	10,20
RU Lupi	0.07	6.39 ± 0.09	0.80	3.00	24	12036	11,18,34
RW Aur A	1.6	5.85 ± 0.53	1.40	3.16	77	11616	1,23,35
SU Aur	0.9	6.39 ± 0.21	2.30	0.45	62	11616	1,17,37
SZ 102	1.13	6.15 ± 0.15	0.75	0.08	10	11616	12,27,38
TW Hya	0.0	7.00 ± 0.40	0.60	0.02	4	8041−*S*	13,18,36
UX Tau A	0.20	6.10 ± 0.30	1.30	1.00	35	11616	1,21
V4046 Sgr	0.0	6.90 ± 0.12	0.86+0.69	1.30	36	11533	14,22,39
V836 Tau	1.70	6.26 ± 0.26	0.75	0.01	65	11616	1,18,41
HBC 427	0.00	6.64 ± 0.14	0.7	⋯	⋯	11616	6
LkCa 19	0.00	6.84 ± 0.38	1.35	⋯	⋯	11616	1
LkCa 4	0.69	6.43 ± 0.25	0.77	⋯	⋯	11616	6
RECX 1	0.00	6.78 ± 0.00	0.90	⋯	⋯	11616	42
TWA 13A	0.00	6.90 ± 0.12	0.32	⋯	⋯	12361	43
TWA 13B	0.00	6.90 ± 0.12	0.38	⋯	⋯	12361	43
TWA 7	0.00	6.39 ± 0.39	0.55	⋯	⋯	11616	44

[a] Targets in the upper group are CTTSs, targets in the lower group are WTTSs.
[b] Program IDs marked −*S* indicate that STIS observations were used

[c] (1) Kraus & Hillenbrand (2009); (2) Ricci et al. (2010), age uncertainties are assumed to be ± 0.20; (3) Alencar et al. (2003); (4) Lawson et al. (1996); (5) Siess et al. (2000); (6) Bertout et al. (2007); (7) Feigelson et al. (2003a); (8) van Boekel et al. (2005); (9) Lawson et al. (2001); (10) Ramsay Howat & Greaves (2007); (11) Herczeg et al. (2005a); (12) Comerón & Fernández (2010); (13) Webb et al. (1999); (14) Quast et al. (2000a); (15) Gullbring et al. (1998); (16) Hartmann et al. (1998); (17) Gullbring et al. (2000); (18) Herczeg & Hillenbrand (2008); (19) Garcia Lopez et al. (2006); (20) Lawson et al. (2004); (21) Andrews et al. (2011); (22) France et al. (2011b); (23) White & Ghez (2001); (24) Gómez de Castro (2009); (25) Espaillat et al. (2007a); (26) Hussain et al. (2009); (27) Comerón et al. (2003a); (28) Andrews & Williams (2007); (29) Johns-Krull & Valenti (2001); (30) Simon et al. (2000); (31) Muzerolle et al. (2003); (32) Espaillat et al. (2010); (34) Stempels et al. (2007); (35) Eisner et al. (2007); (36) Pontoppidan et al. (2008b); (37) Akeson et al. (2002); (38) Coffey et al. (2004); (39) Rodriguez et al. (2010); (40) Grady et al. (2004); (41) Najita et al. (2008); (42) Ingleby et al. (2011b); (43) Plavchan et al. (2009); (44) Neuhäuser et al. (2000); (45) Ingleby et al. (2011a)

from sub-mm/IR interferometric studies, 2) ages, stellar masses, and extinctions were derived from pre-main-sequence stellar evolutionary tracks, and 3) mass accretion rates were derived from measurements of the accretion luminosity. Of our 34 targets, 27 are considered CTTSs while 7 do not show evidence for active accretion or a gas-rich circumstellar disk and are classified as Weak-lined T Tauri Star (WTTSs). These populations are separated as the upper and lower groups, respectively, of target stars listed in Table 1. 7 of the CTTSs in our sample are considered transitional systems (CS Cha, DM Tau, GM Aur, UX Tau A, LkCa15, HD 135344B and TW Hya), with mid-IR SEDs indicating that a gap has opened in their inner dust disks. This sample includes several of the best-studied transitional disks in the literature. References are listed in Table 1, and a more detailed description of a subsample of these targets can be found in Schindhelm et al. (2012a).

The assumed distances are not critical to the results presented here, but they do impact the comparison of the H$_2$, Lyα, and C IV luminosities presented in §4. For the Taurus-Auriga targets (AA Tau, BP Tau, DE Tau, DF Tau, DK Tau, DM Tau, DN Tau, DR Tau, GM Aur, HN Tau, IP Tau, LkCa15, RW Aur, SU Aur, UX Tau A, V836 Tau, HBC 427 (V397 Tau), LkCa19, LkCa4), we assumed d = 140 pc (Elias 1978; Kenyon & Hartmann 1995; and see also the VLBA work presented by Loinard et al. 2007); for the η Cha targets (RECX-11, RECX-15, RECX-1), we assumed $d = 97$ pc (Mamajek et al. 1999); for the TW Hya association targets (TW Hya, TWA13A, TWA13B, TWA7), we assumed $d = 54$ pc (van Leeuwen 2007), and for Chamaeleon I (CS Cha, CV Cha), we assumed $d = 160$ pc (Luhman 2004). Other objects are V4046 Sgr ($d = 83$ pc; Quast et al. 2000), SZ 102 (in Lupus 3, $d = 200$ pc; Comerón et al. 2003), HD104237 (a member of the ϵ Cha group, $d = 116$ pc; Feigelson et al. 2003), AK Sco ($d = 103$ pc; van Leeuwen 2007), and RU Lupi ($d = 121$ pc; van Leeuwen et al. 2007). Six of the

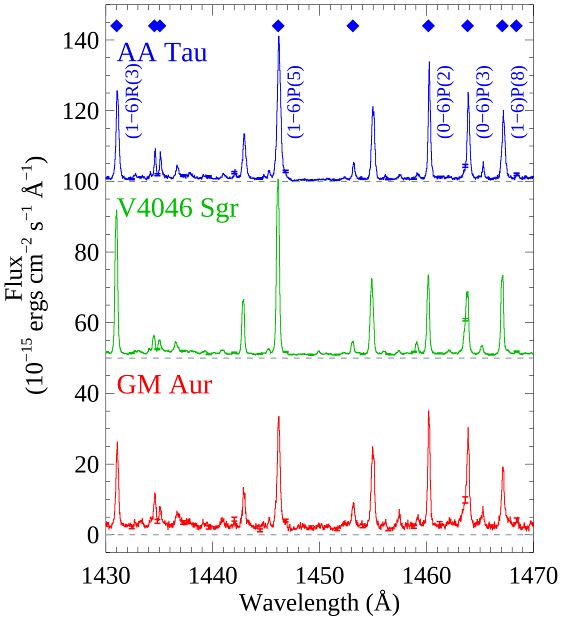

Fig. 2.— The 1430 – 1470 Å spectral region for the gas-rich targets plotted in Figure 1. All of the strong spectral features in this bandpass are emission lines from Lyα-pumped fluorescent H_2. Emission lines used in this analysis are marked with blue diamonds and several bright features are labeled. Objects are plotted in order of decreasing near-IR dust excesses: AA Tau (primordial, n_{13-31} = -0.51; Furlan et al. 2009), V4046 Sgr (pretransitional) has a sub-AU scale hole in the inner disk dust distribution (Jensen & Mathieu 1997), and GM Aur (transitional, n_{13-31} = 1.75; Furlan et al. 2009) has a ∼ 24 AU hole in the inner dust disk (Calvet et al. 2005). The spectra are binned to ≈ 1/2 of a spectral resolution element (3 pixels), and representative error bars are shown overplotted. The H_2 spectra are qualitatively similar, independent of the inner disk dust properties.

nineteen sources in Taurus-Auriga are known multi-star systems (see, e.g., Kraus et al. 2012) and V4046 Sgr is known to be a short-period binary system (Quast et al. 2000b).

2.2. *Observations*

Our sample of 34 T Tauri stars was assembled from new and archival observations with *HST*-COS and -STIS. The majority of the targets were observed as part of the DAO of Tau guest observing program (PID 11616; PI - G. Herczeg) and the COS Guaranteed Time Observing program (PIDs 11533 and 12036; PI - J. Green). Additional observations of the transitional disk HD135344B and weak-lined systems TWA13A and TWA13B (PIDs 11828 and 12361; PI - A. Brown) are presented. A subset of the H_2 survey observations have been presented previously in the literature (France et al. 2011b,a, 2012; Ingleby et al. 2011b; Yang et al. 2011; Schindhelm et al. 2012a). Finally, we have included archival STIS observations of the well-studied CTTS TW Hya (Herczeg et al. 2002), obtained through StarCAT (Ayres 2010).

Most of the targets were observed with the medium-resolution far-UV modes of COS (G130M and G160M; Green et al. 2012). These observations were acquired between 2009 December and 2011 September. Multiple central wavelength settings at several focal-plane split positions were used to create continuous far-UV spectra from ≈ 1150 – 1750 Å and mitigate the effects of fixed pattern noise. These modes provide a point-source resolution of $\Delta v \approx 17$ km s^{-1} with 7 pixels per resolution element (Osterman et al. 2011). The data were smoothed by three pixels for analysis. The total far-UV exposure times were between two and four orbits per target, depending on the intrinsic luminosity and the interstellar plus circumstellar reddening on the sightline. The one-dimensional spectra produced by the COS calibration pipeline, CALCOS, were aligned and coadded using the custom software procedure described by Danforth et al. (2010). The full far-UV spectra of three CTTSs (AA Tau, V4046 Sgr, and GM Aur) and one WTTS (LkCa19) are displayed in Figure 1, and a 40 Å blow-up of the CTTSs is shown in Figure 2.

TABLE 2
Selected H_2 Emission Lines.

Line ID[a]	$[v^{'},J^{'}]$	λ_{lab} (Å)	B_{mn}[b]	λ_{pump} (Å)
(3 – 9)P(14)	[3,13]	1608.33	0.139	1213.36
(3 – 10)R(12)	[3,13]	1615.43	0.125	1213.36
(4 – 6)R(12)	[4,13]	1415.33	0.037	1213.68
(4 – 8)R(12)	[4,13]	1509.45	0.023	1213.68
(4 – 11)R(12)	[4,13]	1613.99	0.092	1213.68
(3 – 5)R(15)	[3,16]	1418.23	0.050	1214.47
(3 – 7)R(15)	[3,16]	1513.99	0.057	1214.47
(3 – 9)R(15)	[3,16]	1593.26	0.122	1214.47
(3 – 10)R(15)	[3,16]	1621.12	0.062	1214.47
(4 – 8)P(5)	[4,4]	1477.05	0.039	1214.78
(4 – 9)P(5)	[4,4]	1526.55	0.033	1214.78
(4 – 11)P(5)	[4,4]	1613.72	0.150	1214.78
(1 – 6)P(8)	[1,7]	1467.08	0.080	1215.73
(1 – 7)R(6)	[1,7]	1500.45	0.101	1215.73
(1 – 7)P(8)	[1,7]	1524.65	0.111	1215.73
(1 – 8)R(6)	[1,7]	1556.87	0.074	1215.73
(1 – 6)R(3)	[1,4]	1431.01	0.058	1216.07
(1 – 6)P(5)	[1,4]	1446.12	0.083	1216.07
(1 – 7)R(3)	[1,4]	1489.57	0.094	1216.07
(1 – 7)P(5)	[1,4]	1504.76	0.115	1216.07
(3 – 7)P(1)	[3,0]	1435.05	0.118	1217.04
(3 – 10)P(1)	[3,0]	1591.32	0.233	1217.04
(3 – 11)P(1)	[3,0]	1636.34	0.099	1217.04
(0 – 5)P(2)	[0,1]	1398.95	0.141	1217.21
(0 – 6)P(2)	[0,1]	1460.17	0.083	1217.21
(0 – 2)P(2)	[0,1]	1521.59	0.032	1217.21
(0 – 5)P(3)	[0,2]	1402.65[c]	0.126	1217.64
(0 – 6)P(3)	[0,2]	1463.83	0.074	1217.64
(0 – 7)P(3)	[0,2]	1525.15	0.029	1217.64
(2 – 5)P(13)	[2,12]	1434.54	0.066	1217.90
(2 – 6)R(11)	[2,12]	1453.10	0.049	1217.90
(2 –8)R(11)	[2,12]	1555.89	0.077	1217.90
(2 – 8)P(13)	[2,12]	1588.80	0.119	1217.90
(2 – 8)P(16)	[2,15]	1612.39	0.138	1218.52
(2 – 9)R(14)	[2,15]	1617.42	0.103	1218.52
(0 – 5)R(2)	[0,3]	1395.20	0.096	1219.09
(0 – 5)P(4)	[0,3]	1407.29	0.120	1219.09
(0 – 6)P(4)	[0,3]	1468.39	0.070	1219.09

[a] Transitions are for the $B^1\Sigma_u^+ - X^1\Sigma_g^+$ H_2 band system.

[b] The branching ratio is the ratio of the line transition probability to the total transition probability out of state $[v^{'},J^{'}]$, $B_{mn} = \frac{A_{n'v'J' \rightarrow v''J''}}{A_{n'v'J'}}$

[c] Blended with Si IV λ_{lab} = 1402.77 Å in some targets.

Targets that exceeded the COS bright-object limit were observed with STIS in the medium-resolution echelle mode. We used the E140M mode ($\Delta v \approx 8$ km s^{-1}) mode through the 0.2″ × 0.2″ slit for exposure times between two and three orbits per object. The far-UV STIS spectra were combined using the STIS echelle soft-

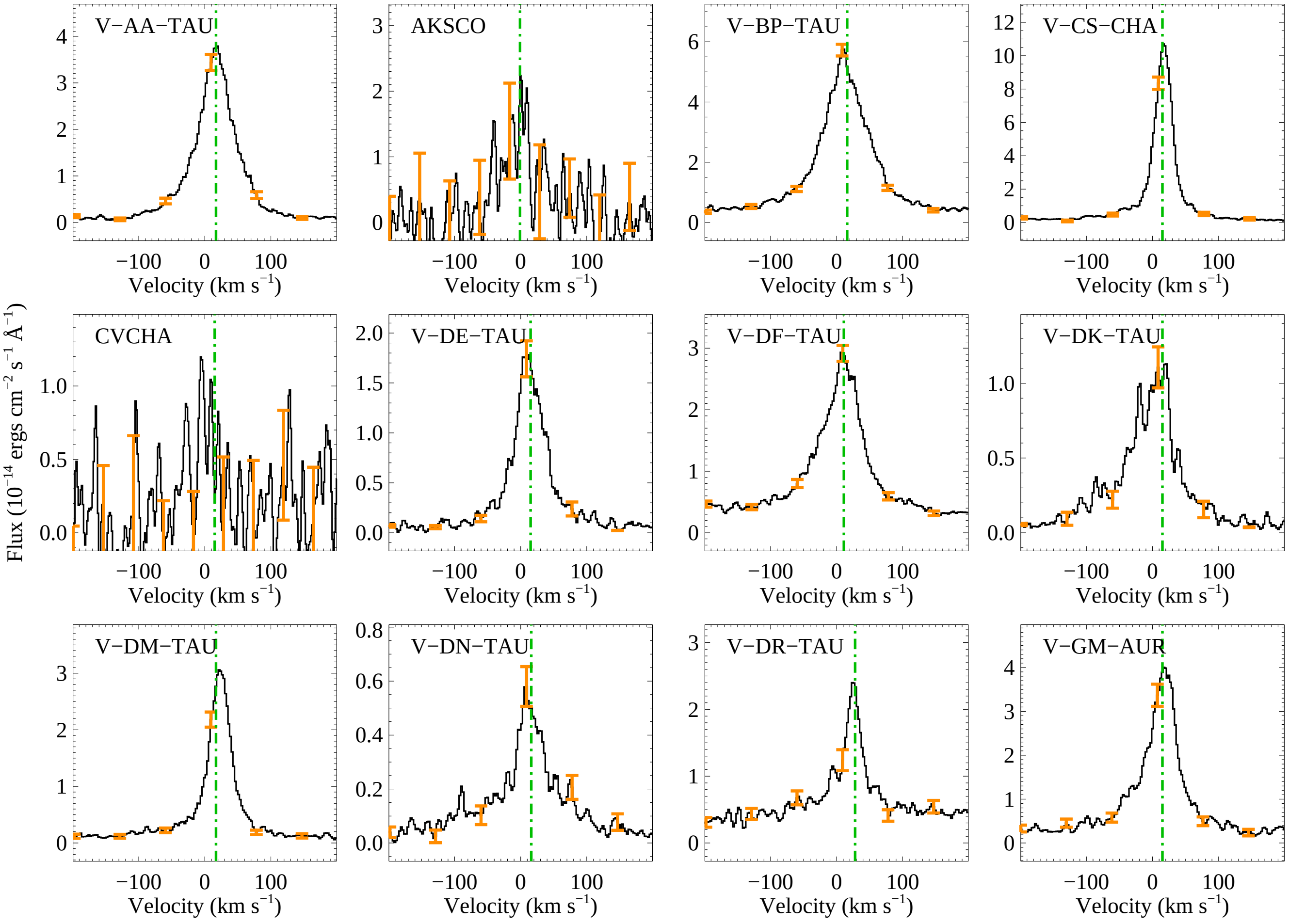

FIG. 3A.— Velocity profiles for the H_2 $B^1\Sigma_u^+ - X^1\Sigma_g^+$ (1 – 7) R(3) (λ_{lab} = 1489.57 Å) emission line in all targets, plotted over the ± 200 km s^{-1} interval. The data plotted here are smoothed to 3 pixels (≈ 0.5 spectral resolution elements), with representative error bars shown in orange. The green dash-dotted line is plotted at the stellar radial velocity, when known. The target labels are the target names identified in the headers of the *HST* spectroscopic observations.

ware developed for the StarCAT catalog (T. Ayres – private communication; Ayres 2010).

3. ANALYSIS

We observe fluorescent H_2 emission from all of the 27 CTTSs in our sample, and no H_2 emission from the 7 WTTS targets. The number of observed fluorescent progressions varies significantly across the sample, and we present our measurements of the total H_2 fluxes below. We detect strong fluorescent emission in all of the transitional objects in our sample (CS Cha, DM Tau, GM Aur, UX Tau A, LkCa15, HD 135344B and TW Hya; §4.3).

The fluorescent H_2 lines observed in the CTTS sample can be used to determine the relative amount of H_2 in the circumstellar environment and to constrain its spatial distribution. For our line-profile analysis, we focus on the measurement of two progressions ($[v^{'},J^{'}]$ = [1,7] and [1,4]) detected in all of the CTTS targets[12]. These emission lines are pumped through the (1 − 2)R(6) λ_{lab}1215.73 Å and (1 − 2)P(5) λ_{lab}1216.07 Å transitions, respectively. The absorbing transitions are within +15 – +100 km s^{-1} of Lyα line-center. The signal-to-noise ratios (S/N) per resolution element are typically between 5 and 40 in the brightest fluorescent H_2 emission lines for our CTTS targets. The (1 − 7)R(3) λ_{lab} = 1489.57 Å transition is relatively free from spectral contamination and is displayed for all targets in Figure 3 ($a - c$). When available, the stellar radial velocities are indicated in Figure 3 with green dash-dotted lines. Within the ∼ 15 km s^{-1} wavelength solution accuracy of COS, most of the H_2 progressions are consistent with the stellar velocity. In several cases the H_2 lines appear to have line wings extending to negative velocities or statistically significant differences in the velocity widths of different H_2 progressions. RW Aur is an extreme example of this behavior. Ardila et al. (2002) and Herczeg et al. (2006) have noted the presence of blue-shifted H_2 emission in their sample

---

[12] The quantum numbers v and J denote the vibrational and rotational quantum numbers in the ground electronic state ($X^1\Sigma_g^+$), the numbers $v^{'}$ and $J^{'}$ characterize the H_2 in the excited ($B^1\Sigma_u^+$) electronic state, and the numbers $v^{''}$ and $J^{''}$ are the rovibrational levels in the electronic ground state following the fluorescent emission. Absorption lines are described by ($v^{'} - v$) and emission lines by ($v^{'} - v^{''}$).

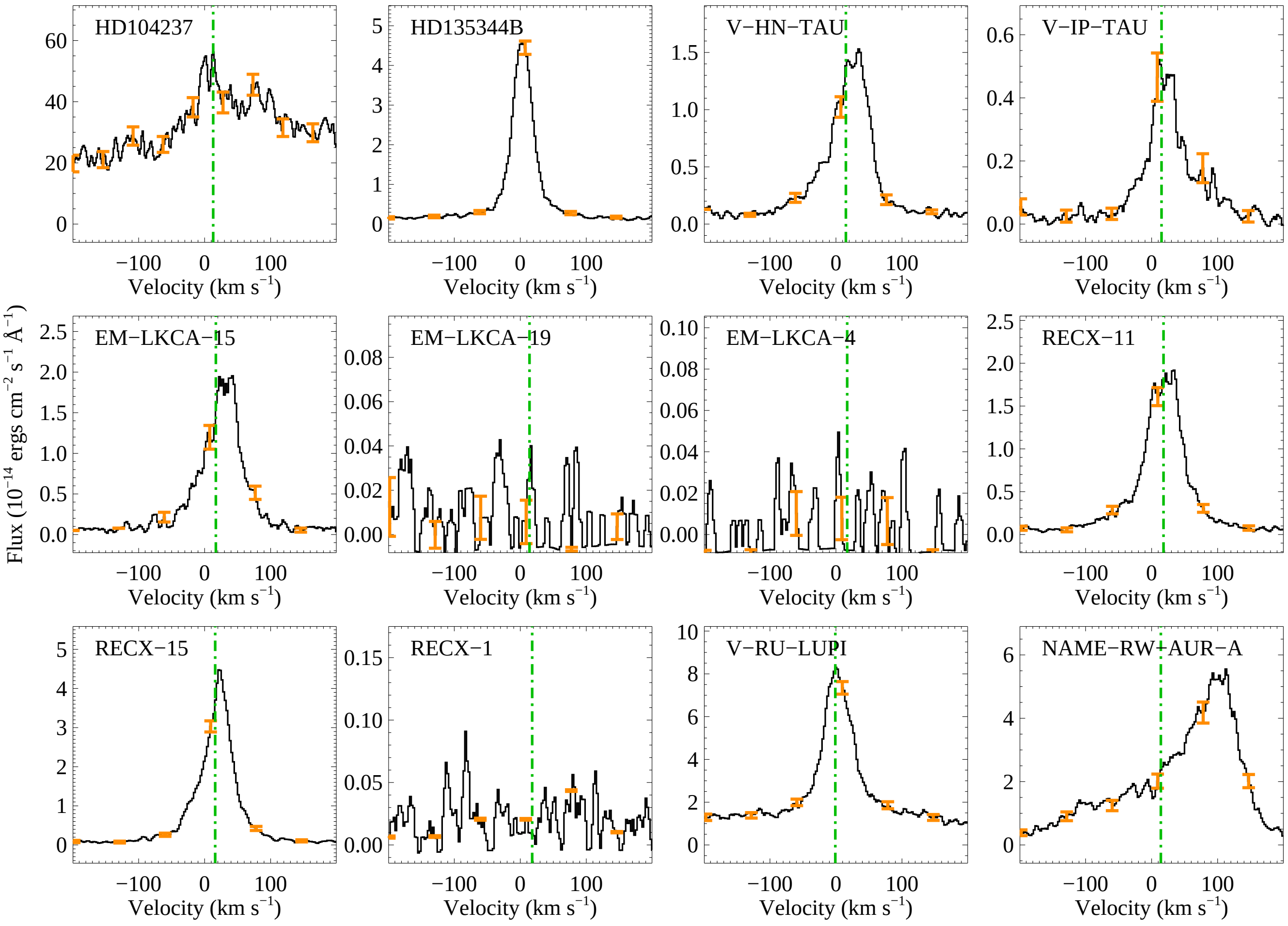

FIG. 3B.— same as Figure 3a.

of T Tauri stars observed with GHRS and STIS. The presence of blue-shifted emission creates additional uncertainty in the measured line-widths at the resolution of our spectra, and we present a discussion of outflow signatures observed in our sample in §4.2.1.

The high S/N of the COS data means that we can restrict the analysis to the brightest lines from the progressions of interest. Systematics were minimized by focusing on emission lines with wavelengths $1395 \lesssim \lambda \lesssim 1640$ Å. This choice is optimal because 1) fluorescent transitions cascading to vibrational levels $v^{\prime\prime} \gtrsim 5$ do not suffer significant self-absorption before escaping the circumstellar environment (e.g., Figure 7 of Herczeg et al. 2004), enabling more robust flux measurements, 2) the non-Gaussian wings of the COS instrumental line-spread function (LSF[13]) contain a smaller fraction of the power at $\lambda > 1400$ Å, 3) the strongest lines from the [1,4] and [1,7] progressions are in this range, and 4) the relative correction for interstellar reddening between the different fluorescent emission lines is minimized. The first and latter two arguments apply equally to the STIS data.

3.1. *Line Fluxes and the H_2 Progression Luminosity*

The H_2 emission lines were fit with an interactive multi-Gaussian IDL line-fitting code optimized for COS emission line spectra. This code assumes a Gaussian lineshape convolved with the wavelength dependent LSF, then uses the MPFIT routine to minimize χ^2 between the fit and data (Markwardt 2009). A second order polynomial background, the Gaussian amplitudes, and the Gaussian FWHMs for each component are free parameters. The parameters of the underlying Gaussian emission lines are returned to the user. The smaller STIS aperture does not sample the broad wings of the *HST* LSF, therefore unconvolved Gaussians were used for the targets observed with STIS. We chose 12 progressions with absorbing transitions that spanned the width of the observed Lyα profiles in most targets, $1213.3 \leq \lambda_{abs}(H_2) \leq 1219.1$ Å (Schindhelm et al. 2012b). We fit the brightest unblended lines from 12 progressions in the 1395 – 1640 Å bandpass, and used these values to determine the total flux from each progression.

A list of the selected lines is given in Table 2. The total

---

[13] The LSF experiences a wavelength dependent non-Gaussianity due to the introduction of mid-frequency wave-front errors produced by the polishing errors on the *HST* primary and secondary mirrors; `http://www.stsci.edu/hst/cos/documents/isrs/`

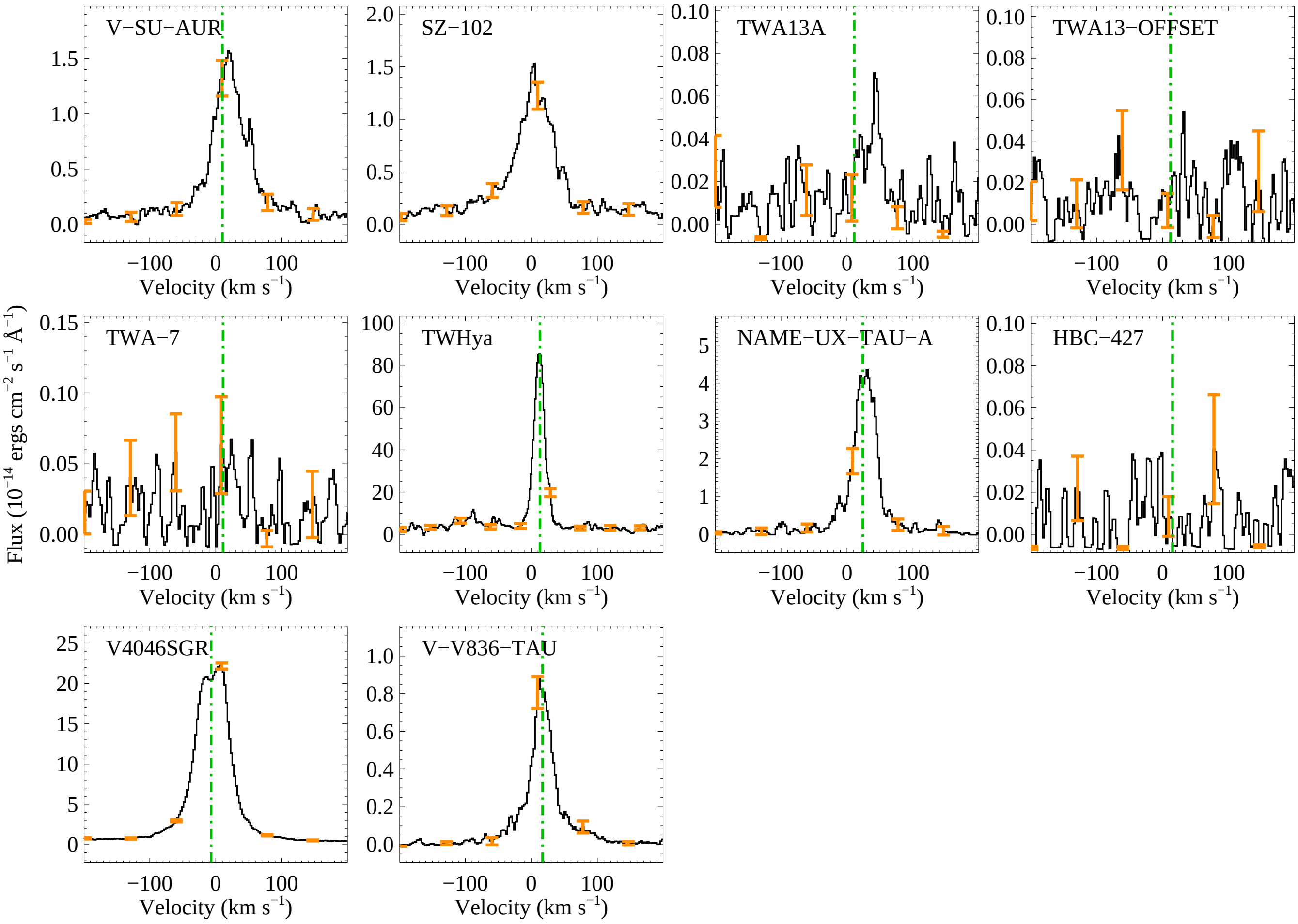

Fig. 3c.— same as Figure 3a.

flux from a given progression is given by

$$F_m(\mathrm{H}_2) = \frac{1}{N}\sum\left(\frac{F_{mn}}{B_{mn}}\right) \qquad (1)$$

where F_{mn} is the reddening corrected, integrated H_2 emission line flux from rovibrational state m $(= [v^{'},J^{'}])$ in the $B^1\Sigma_u^+$ electronic state to n $(= [v^{''},J^{''}])$ in the ground electronic state, $X^1\Sigma_g^+$. B_{mn} is the branching ratio between these two states, and N is the number of emission lines measured from a given progression. The measurement errors are typically small, so we take the flux error to be the standard deviation of the individual measurements of $F_m(\mathrm{H}_2)$. The dominant systematic error on the measured H_2 flux is the correction for interstellar reddening; we do not attempt to account for this uncertainty in the flux and luminosity errors presented below. See the ApJ version of this paper (or contact the authors) for reddening-corrected progression fluxes for all of the gas-rich targets. The total progression luminosity is then $L_m(\mathrm{H}_2) = (4\pi d^2)F_m(\mathrm{H}_2)$. Upper limits on the H_2 emission line fluxes in the gas-depleted targets were determined from the standard deviation in a ± 50 km s^{-1} region surrounding the laboratory wavelength of the transition. The total fluorescent H_2 luminosity is then taken as the sum of all 12 of the fluorescent progressions. This prescription should account for $\gtrsim$ 80 % of the total Lyα-pumped H_2 emission from our targets, although the exact fraction of the total measured H_2 flux will depend on the local Lyα line-profile (Herczeg et al. 2004; Schindhelm et al. 2012b).

Depending on the geometry and spatial distribution of the absorbing molecular layer, the H_2 absorption lines may be optically thin (or have optical depths of a few) in some targets. In this case, the emitted H_2 luminosity will be directly proportional to the number of Lyα pumping photons received. Schindhelm et al. (2012b) have presented total incident Lyα fluxes for 14 of the targets in our sample. Using a line-profile reconstruction technique that takes into account the 12 H_2 progressions described above, they simultaneously fit the neutral hydrogen outflow, the H_2 column density, and the H_2 temperature (previous examples of H_2-based Lyα reconstructions are described by Wood et al. 2002; Wood & Karvoska 2004; Herczeg et al. 2004). The amount of the stellar Lyα that is redistributed by H_2 can be determined by dividing the total H_2 flux, $F(\mathrm{H}_2)$, by the total Lyα flux, $F(\mathrm{H}_2)/F(\mathrm{Ly}\alpha)$. The H_2 luminosity can also be compared to accretion indicators in our data set, such as C IV. Emission from the C IV $\lambda\lambda$1548,1550 Å

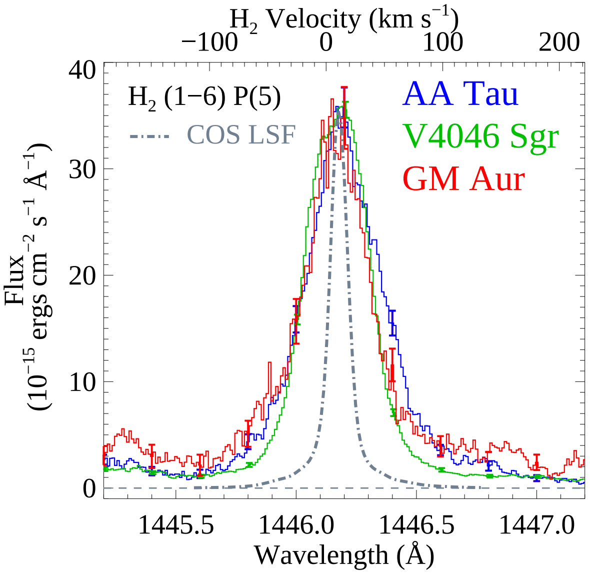

FIG. 4.— Expanded view of the H$_2$ $(1-6)$ P(5) ($\lambda_{lab} = 1446.12$Å) emission line, showing the velocity width beyond the COS line-spread function (shown as the gray dash-dotted line) for the three example targets shown in Figure 2. The AA Tau and V4046 Sgr spectra have been normalized to the peak flux of the GM Aur H$_2$ emission and shifted to the centroid velocity of the H$_2$ emission. The emission lines are spectrally resolved by COS.

resonance doublet in excess of a baseline magnetospheric level has been shown to correlate with the mass accretion rate (Johns-Krull et al. 2000; Yang et al. 2012). The C IV flux can be measured directly in the same data set from which we measure F_m(H$_2$), mitigating complications associated with short- and long-baseline time variability. Due to the non-Gaussian appearance of many of the C IV emission profiles, we measured F(C IV) by integrating the reddening corrected spectra over (1547.5 – 1553.5 Å) and subtracted the continuum from an adjacent, line-free portion of the spectrum.

3.2. *H$_2$ Line Widths and the Average H$_2$ Radius, $\langle R_{H2}\rangle$*

Figure 4 shows the H$_2$ $(1-6)$P(5) ($\lambda_{lab} = 1446.12$ Å) profiles of the three example spectra displayed in Figure 2, with the 1450 Å *HST*+COS LSF overplotted as the gray dash-dot line. These spectra are typical of the CTTS sample and one observes that the emission lines are spectrally resolved. We display the basic H$_2$ and C IV line parameter observations for the [1,7] and [1,4] progressions in Figure 5. The H$_2$ emission line FWHMs are uncorrelated with the stellar mass, F_m(H$_2$), or F(C IV).

Kinematic broadening dominates the observed H$_2$ line profiles (see §4.2). The thermal broadening of the emission lines is approximately 4.5 km s^{-1} at the nominal 2500 K H$_2$ layer, significant additional broadening would require temperatures in excess of the $\approx$ 4500 K dissociation temperature of H$_2$ (Lepp & Shull 1983). If we further assume that any turbulence in the disks is subsonic, then the maximum turbulent velocity will be no larger than a few km s^{-1}. Therefore, velocity broadening due to bulk motions and Keplerian rotation dominate the observed line shapes when the FWHM of the emission line is greater than the 17 km s^{-1} spectral resolution of COS. For the case of H$_2$ in a circumstellar disk, we define a simple metric to characterize the average H$_2$ radius, $\langle R_{H2}\rangle$,

$$\langle R_{H2}\rangle_m = GM_* \left(\frac{2sin(i)}{FWHM_m}\right)^2 \tag{2}$$

where M_* is the stellar mass, i is the inclination angle, and FWHM$_m$ is the mean of the Gaussian FWHMs for a given progression m. This definition of the average molecular radius is analogous to the UV-CO radius used by Schindhelm et al. (2012a). When possible, we use disk inclinations derived from the sub-mm dust continuum observations presented by Andrews & Williams (2007) and Andrews et al. (2011). In principle, the error on the average H$_2$ radius should include uncertainties on the stellar mass and disk inclinations, however these uncertainties are not available for all targets. Therefore, the quoted error on $\langle R_{H2}\rangle$ only includes measurement uncertainties from the H$_2$ line fitting.

In Table 3 we present $\langle R_{H2}\rangle$ for the $[v^{'}, J^{'}] = [1,7]$ progression ($\equiv \langle R_{H2}\rangle_{[1,7]}$). We focus on the [1,7] progression due to its proximity to the Lyα line-center. This progression should be one of the most readily observable in weakly accreting systems because as the accretion-powered Lyα flux decreases, the flux in the wings of Lyα may be insufficient to excite a detectable level of H$_2$ emission. However, the [1,7] progression should continue to be observable even in systems with narrow Lyα profiles (e.g., France et al. 2010). While we concentrate on the $\langle R_{H2}\rangle_{[1,7]}$, the $\langle R_{H2}\rangle_{[1,4]}$ distribution is qualitatively similar. We do not compute $\langle R_{H2}\rangle$ for targets with inclination angles $< 15°$; the small radial component of the H$_2$ velocity vector makes the derived radii very sensitive to uncertainties in the disk geometry. We also do not compute $\langle R_{H2}\rangle$ for the only unambiguously outflow-dominated source in the sample, RW Aur (§4.2.1). The impact of a second, weaker outflow emission component will bias our results towards smaller H$_2$ radii in some targets, but a single component dominates the majority of our sources, therefore we adopt a single emission component in order to facilitate a uniform spectral analysis.

A knowledge of the inner disk radius, R_{in}, is important for understanding the star-disk interaction. In order to avoid complications from outflows or blending from adjacent weaker H$_2$ transitions, we do not measure R_{in}(H$_2$) from half-width zero-intensities (HWZI, e.g., Brittain et al. 2009). Instead, we adopt the definition of R_{in} suggested by Salyk et al. (2011a) for mid-IR CO emission from the inner disk, where R_{in} is the Keplerian semi-major axis corresponding to 1.7 × HWHM of the Gaussian line fit. This choice leads to the relation between the average H$_2$ radius and the inner H$_2$ radius, $\langle R_{H2}\rangle_{[1,7]} = 2.89\ R_{in}$(H$_2$). R_{in}(H$_2$) is given with $\langle R_{H2}\rangle_{[1,7]}$ in Table 3.

4. DISCUSSION

There are numerous indicators of the gas and dust content of a young protoplanetary system. Three important observables are the warm dust content of the inner disk, the presence of circumstellar gas, and signs of active accretion. Our *HST* observations provide measurements of the last two, while the first has been extensively studied in the IR. The combination of low spectral resolution and large instrumental backgrounds that have complicated the detection and analysis of H$_2$ in previous UV

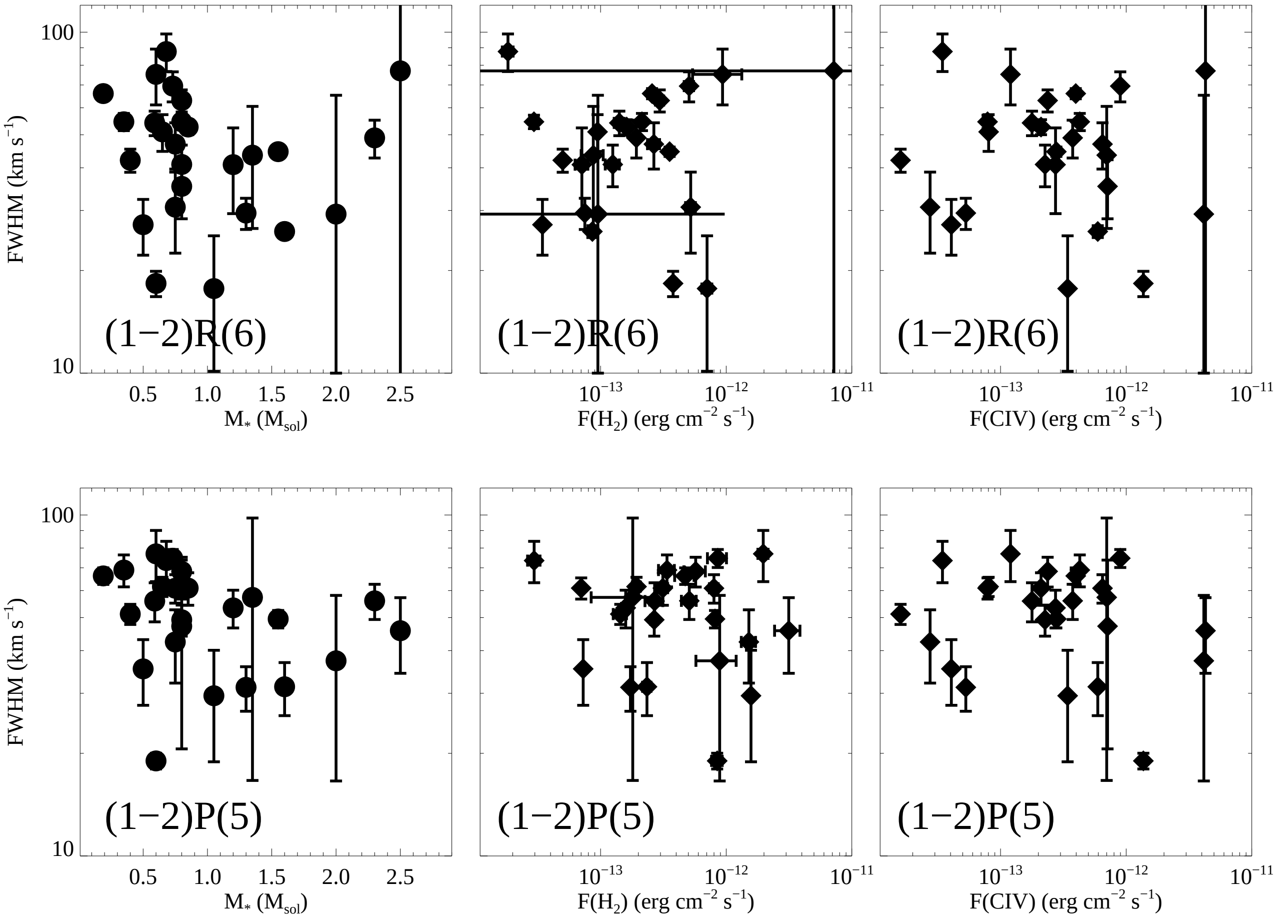

Fig. 5.— The average H_2 FWHM is compared with the stellar mass, the progression flux ($F_m(H_2)$), and the C IV flux (F(C IV)) for two progressions: [1,7] (pumped through the (1 − 2) R(6) λ_{lab} = 1215.73Å transition) and [1,4] (pumped through the (1 − 2) P(5) λ_{lab} = 1216.07Å transition). The H_2 emission line FWHMs are uncorrelated with the stellar mass, $F_m(H_2)$, or F(C IV).

surveys has largely been remedied with the installation of COS. The large transition probabilities of the H_2 electronic band systems and the lack of photospheric emission at $\lambda < 1700$ Å in low-mass stars make fluorescent H_2 one of the most sensitive indicators for the presence of molecular gas in the inner ~ 10 AU of young circumstellar disks.

Accretion shocks are a significant source of hot gas in accreting systems, observed as UV and X-ray emission lines in excess of what can be attributed to magnetospheric activity alone (Calvet & Gullbring 1998; Johns-Krull et al. 2000; Günther & Schmitt 2008). Specifically, excess emission from neutral hydrogen (line formation temperature $T_{form} \sim 10^4$ K; observed as Lyα and Hα emission) and the C^{3+} ion ($T_{form} \sim 10^5$ K; observed through the $\lambda\lambda$ 1548, 1550 Å C IV resonance doublet) correlate well with both the mass accretion rate and the H_2 emission from the system (Johns-Krull et al. 2000). This supports a symbiotic picture where gas-rich disks provide fuel for active accretion, and that accretion dominates the production of the Lyα photons that make the H_2 disk detectable.

The total H_2 luminosity is compared with the Lyα and C IV luminosities in Figure 6. The general trend follows the expected relation that systems with larger L(Lyα) and L(C IV) are actively accreting gas-rich disks. Lyα fluxes are only available for about half of our sample (see Schindhelm et al. 2012b), and we interpolate (or extrapolate) the strong correlation between F(Lyα) and $F(H_2)$ to estimate L(Lyα) for the remaining objects. The direct measurements are shown as black squares in Figure 6, the interpolated (extrapolated) values are shown in green, and upper limits are indicated in red. The correlation between $L(H_2)$ and L(C IV) has a spread of $\sim 1 - 1.5$ orders of magnitude in $L(H_2)$ at a given C IV luminosity. This spread may be partially due to uncertainties in the distance and reddening correction used to derive the luminosities, disks/outflows with differing amounts of molecular gas, and intrinsic variations in the C IV flux. In the following subsections, we combine our molecular and atomic tracers to constrain the properties of H_2 in the circumstellar environments of these systems.

4.1. *Evolution of the H_2 Luminosity and Reprocessing of the Lyα Radiation Field*

The dissipation of inner dust disks (at $a < 1$AU) is thought to be mostly complete by ≈ 6 Myr (e.g., Haisch et al. 2001; Wyatt 2008 and references therein). If the molecular gas and dust are coupled, we would expect

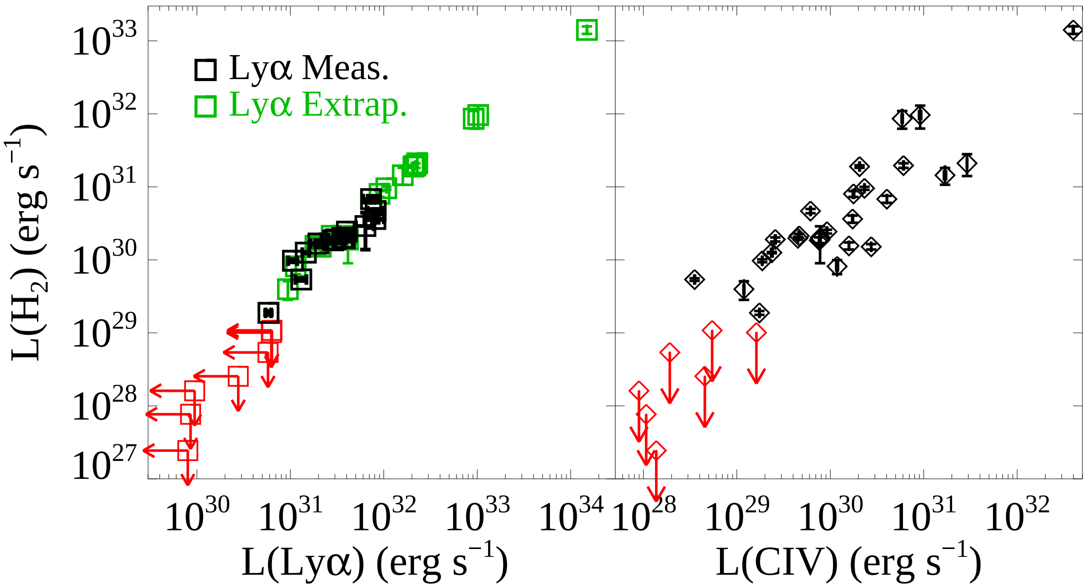

Fig. 6.— A comparison of the hot gas [$\log_{10}(T_{form}) \sim 4 - 5$] and molecular gas emission from the TTSs studied here. The Lyα and C IV emission is produced in the protostellar atmosphere through a combination of magnetic activity and magnetically funneled accretion. The H_2 resides in the circumstellar disk and in some cases, extended outflows, excited by Lyα photons. The H_2 luminosity is the summed luminosity of the 12 progressions listed in Table 2, representing $\gtrsim$ 80% of the total H_2 luminosity (depending on the specific Lyα pumping profile). Targets with H_2 upper limits are plotted in red. The black squares in the left plot are our H_2 measurements and the empirically determined Lyα fluxes presented by Schindhelm et al. (2012b). The green squares are an extrapolation of the $F(H_2)$ vs. F(Lyα) relationship.

to observe a decrease in the H_2 content as a function of system age. The evolution of the H_2 luminosity is plotted in the top panel of Figure 7. The H_2 detections are shown in black and the non-detections in red. The total H_2 luminosity decreases with time, in agreement with the findings of Ingleby et al. (2009, 2011a). However, the large scatter in the relation prevents one from inferring a characteristic timescale for this decrease. The dominant sources of uncertainty in this relation are the correlated errors on the age and extinction. The observed decrease in $L(H_2)$ as a function of time does not necessarily correspond to a monotonic decrease in the H_2 content. We expect that the Lyα luminosity should track the accretion rate (e.g. Fang et al. 2009 demonstrate the correlation between accretion and H Balmer emission), therefore as the accretion rates decline over time (Armitage et al. 2003; Sicilia-Aguilar et al. 2010), the associated reduction in Lyα emission could mimic the effect of H_2 dissipation with age. The true situation is likely a combination of these effects: gas disk dissipation leads to lower accretion rates that in turn produce fewer Lyα photons to pump the observed fluorescence.

The lower panel in Figure 7 shows the ratio of the H_2 flux and the Lyα flux as a function of system age for the 14 objects with computed Lyα fluxes (Schindhelm et al. 2012b). This plot shows the fraction of the stellar + shock Lyα that is reprocessed by H_2. The actual reprocessing factor is $\eta F(H_2)/F(\mathrm{Ly}\alpha)$, where η is a correction factor to account for anisotropies in the system geometry and fluorescent radiative transfer (Wood et al. 2002; Wood & Karovska 2004). In the case of isotropic emission, η is simply the geometric filling fraction of the H_2, as seen by the Lyα photons. For this comparison (and for the computation of L(Lyα) in Figure 6), we have assumed $\eta = 1$. For sources where the majority of the H_2 resides in a flattened disk, η is most likely less than one (Herczeg et al. 2004 found $\eta \approx 0.25$ in model fits to the spectrum of TW Hya), while for sources with a significant outflow component η may be ~ 1. Yang et al. (2011) and France et al. (2012) present analyses of H_2 absorption lines imposed on the Lyα profiles of the CTTSs V4046 Sgr, DF Tau, and AA Tau, systems with both high and low inclinations. This implies that at least some portion of the H_2 in these systems has a Lyα covering fraction of near unity, suggesting that $\eta \sim 1$ even in some disk-dominated systems. Furthermore, in cases where Lyα has been scattered out of our line of sight or self-absorption redistributes the fluorescence to the higher v'' levels we use to determine $F(H_2)$, η can be > 1 (Wood et al. 2002). In the absence of a more sophisticated radiative transfer treatment of each system individually, we assume $\eta = 1$ for the present analysis.

The total Lyα flux is the full, unabsorbed Lyα profile as it is emitted from the immediate stellar environment. Figure 7 shows that the ratio of the total emitted Lyα flux that is reprocessed by H_2 is 6.2 ± 2.1%. A more meaningful measure of the degree of H_2 reprocessing is the ratio of incident Lyα that arrives at

TABLE 3
Molecular and Atomic Emission Line Parameters.

Target	$\mathrm{FWHM}_{[1,7]}$[a] (km s^{-1})	$\langle R_{H2}\rangle_{[1,7]}$[a] (AU)	R_{in}[b] (AU)	FWHM_{CO}[c] (km s^{-1})	n_{13-31}	$L(H_2)$[a] (10^{29} erg s^{-1})	$L(\mathrm{Ly}\alpha)$[d] (10^{29} erg s^{-1})	L(C IV)[e] (10^{29} erg s^{-1})
AATAU	62 ± 4	0.69 ± 0.08	0.24	92	-0.51	46.7 ± 3.1	818.5 ± 146.6	6.1
AKSCO	57 ± 35	1.25 ± 0.77	0.43	···	···	8.1 ± 1.3	114.4	11.8
BPTAU	70 ± 6	0.13 ± 0.02	0.05	87	-0.58	68.0 ± 7.4	731.7 ± 129.7	40.3
CSCHA	18 ± 7	9.00 ± 4.55	3.11	···	2.89	189.9 ± 12.9	2076.7	20.6
CVCHA	22 ± 30	4.75 ± 3.88	1.64	···	-0.27	139.1 ± 35.5	1540.7	169.1
DETAU	55 ± 6	0.23 ± 0.04	0.08	···	-0.12	20.1 ± 3.0	361.2 ± 106.0	7.8
DFTAU[f]	64 ± 7	0.16 ± 0.03	0.06	79	-1.09	95.7 ± 4.6	1064.7	23.2
DKTAU [f]	55 ± 2	0.24 ± 0.02	0.08	···	-0.81	21.3 ± 1.2	276.7	4.6
DMTAU	27 ± 5	0.80 ± 0.24	0.28	···	1.30	9.7 ± 0.7	106.5 ± 11.7	1.9
DNTAU	71 ± 19	0.09 ± 0.04	0.03	···	-0.43	210.6 ± 67.8	2279.5	290.8
DRTAU	35 ± 7	2.09 ± 0.62	0.72	29	-0.40	14117.7 ± 1590.0	149385.1	3986.7
GMAUR	41 ± 11	1.68 ± 0.65	0.58	47	1.76	18.5 ± 1.8	286.1 ± 70.4	7.6
HD104237	94 ± 77	0.10 ± 0.07	0.03	···	···	964.4 ± 315.6	10239.6	91.6
HD135344B	26 ± 1	···	···	47	···	15.1 ± 1.3	212.0	27.4
HNTAU[f]	61 ± 17	0.47 ± 0.18	0.16	···	-0.44	19.1 ± 1.1	307.2 ± 60.3	2.6
IPTAU[f]	102 ± 29	0.17 ± 0.07	0.06	···	-0.11	4.0 ± 0.2	94.0	1.2
LkCa15	53 ± 3	0.62 ± 0.06	0.21	···	0.62	24.4 ± 1.3	403.4 ± 66.4	9.2
RECX11	54 ± 3	0.85 ± 0.08	0.29	···	···	1.9 ± 0.1	58.3 ± 3.9	1.7
RECX15[f]	41 ± 4	0.62 ± 0.10	0.21	···	···	5.4 ± 0.3	130.6 ± 17.8	0.4
RULUPI	40 ± 2	0.30 ± 0.03	0.10	24	···	27.2 ± 15.2	635.3 ± 148.3	12.0
RWAUR[g]	···	···	···	···	-0.54	860.7 ± 228.9	9169.5	58.9
SUAUR	49 ± 6	2.67 ± 0.58	0.92	121	0.74	36.3 ± 4.0	811.4 ± 191.4	17.3
SZ102	47 ± 7	···	···	···	···	196.2 ± 13.8	2182.4	60.8
TWHYA	18 ± 2	···	···	17	···	16.8 ± 2.0	199.6 ± 34.3	17.0
UXTAU	29 ± 3	1.76 ± 0.33	0.61	21	1.83	12.6 ± 0.3	146.3 ± 12.3	2.4
V4046SGR	45 ± 1	0.95 ± 0.06	0.33	···	···	19.8 ± 0.9	383.3 ± 42.1	4.5
V836TAU	47 ± 20	0.99 ± 0.50	0.34	···	-0.45	80.2 ± 7.3	900.5	17.7
HBC427[h]	···	···	···	···	···	$\lesssim$ 0.5	$\lesssim$ 57.7	0.2
LKCA19	···	···	···	···	···	$\lesssim$ 1.1	$\lesssim$ 63.6	0.5
LKCA4	···	···	···	···	···	$\lesssim$ 1.0	$\lesssim$ 62.6	1.6
RECX1	···	···	···	···	···	$\lesssim$ 0.3	$\lesssim$ 27.7	0.5
TWA13A	···	···	···	···	···	$\lesssim$ 0.1	$\lesssim$ 9.2	0.1
TWA13B	···	···	···	···	···	$\lesssim$ 0.2	$\lesssim$ 10.2	0.1
TWA7	···	···	···	···	···	$\lesssim$ 0.0	$\lesssim$ 8.6	0.1

[a] Average FWHM and average H_2 radius (see §3.2) were calculated from four lines of the H_2 $B^1\Sigma_u^+ - X^1\Sigma_g^+$ $(1 - v'')$ R(6)+P(8) progression. The H_2 luminosity is the sum of the 12 progressions measured in this work (Table 2).

[b] Inner H_2 radius, defined as $R_{in} = GM_* \, (\sin(i)/(1.7 \times \mathrm{HWHM}_{[1,7]}))^2$.

[c] CO line-widths taken from Salyk et al. (2011a) and Bast et al. (2011).

[d] H I Lyα luminosities with error bars were calculated from the Lyα fluxes presented by Schindhelm et al. (2012b). Values without error bars were extrapolated from the relationship between $F(H_2)$ and $F(\mathrm{Ly}\alpha)$.

[e] Measurement error on the C IV flux is taken as 5%.

[f] Targets where molecular outflows may contribute to the observed H_2 line-width.

[g] Strong molecular outflows in RW Aur contaminate the Gaussian fitting (see Figures 3*b* and 8).

[h] Targets below the double line do not show measurable H_2 emission in their far-UV spectra.

the molecular material. The Lyα profile will experience some degree of absorption in the circumstellar environment prior to reaching the molecules (Wood & Karovska 2004; Herczeg et al. 2004; Schindhelm et al. 2012a). Using the incident Lyα profile observed by the H_2, we find that the reprocessing fraction $(\eta F(H_2)/F(\mathrm{Ly}\alpha))$ is 11.5 ± 1.8%. Therefore, modulo the factor of η, we infer that H_2 is capable of reprocessing $> 10\%$ of the incident Lyα flux. This is interesting because the H_2 *a*) will isotropically redistribute the Lyα photons and *b*) represents a means for transferring Lyα photons out of the Lyα line-core and redistributing them across the $1000 \lesssim \lambda \lesssim 1650$ Å bandpass. Additionally, H_2 scattering is a means for redirecting Lyα photons initially on a grazing incidence trajectory, increasing the far-UV radiation penetration depth. This will significantly alter the radiative transfer of this fraction of the Lyα energy as it diffuses outward and downward through the disk (Fogel et al. 2011; Bethell & Bergin 2011). The transfer of these H_2-redistributed Lyα photons will be regulated by circumstellar grains, and this process will add power to discrete wavelengths in the far-UV spectrum that propagates towards the disk midplane, possibly perturbing disk chemistry in regions of active planet formation.

4.2. *Spatial Distribution of H_2*

4.2.1. *H_2 Outflows*

A single Gaussian emission line describes many of the observed velocity profiles, however several targets show evidence for molecular outflows in the form of additional red/blue-shifted H_2 emission. Beck et al. (2008) presented an outflow-selected sample of CTTSs that display spatially extended near-IR rovibrational H_2 spectra. Furthermore, Pontoppidan et al. (2011) have found slow (5 − 10 km s^{-1}), weakly collimated molecular winds to be common in CO spectra of CTTSs, and varying contributions from these winds/outflows could be responsible for the blue-shifted H_2 that is observed towards some systems. The COS observations of DF Tau, DK Tau,

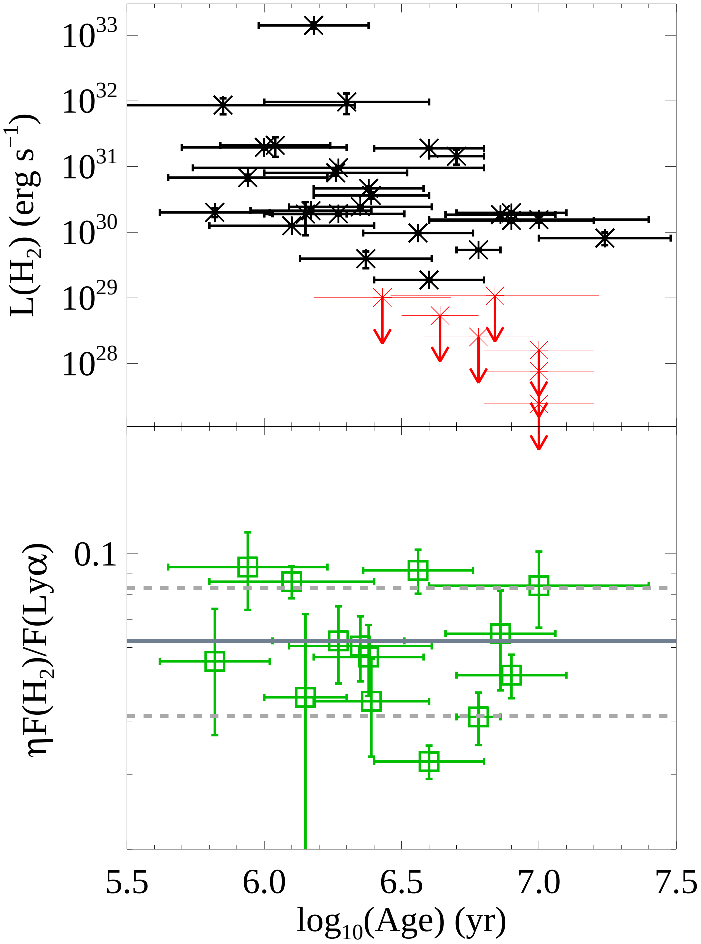

FIG. 7.— We plot the time evolution of the H_2 luminosity from the protoplanetary environment (*top*). The H_2 detections are shown in black and the non-detections in red. The lower plot presents a measure of the H_2 reprocessing of the stellar Lyα emission, expressed as the H_2 flux, divided by the empirically determined photo-exciting Lyα fluxes (Schindhelm et al. 2012b). η is a correction for radiative transfer effects and the anisotropy of the system, set here to $\eta = 1$ (see §4.1). The average H_2 reprocessing fraction of the total Lyα profile is 6.2 ± 2.1 %, assuming $\eta = 1$, shown with solid (mean) and dashed (1 σ) gray lines in the lower panel.

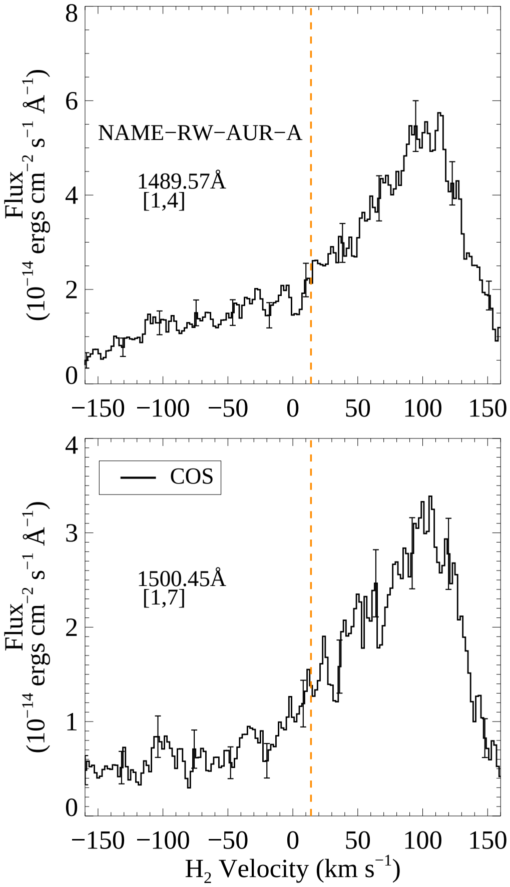

FIG. 8.— COS H_2 line profiles of RW Aur display a complicated kinematic behavior. Stellar variability compromises radial velocity measurements for RW Aur. We display +14 km s^{-1}, the canonical stellar radial velocity (Hartmann et al. 1986), as the dashed orange line. The H_2 line profile is dominated by the redshifted outflow lobe (Melnikov et al. 2009) with an outflow velocity of ≈ 100 km s^{-1}.

HN Tau, LkCa15, IP Tau, RECX-15, RU Lupi, and RW Aur all display H_2 line wings extending to the blue of the stellar radial velocity. Interestingly, half of these objects are known binaries (DF Tau, DK Tau, HN tau, and RW Aur), and this may indicate that interactions with a companion star contribute to the generation of molecular outflows in CTTSs. Clearly, more data is required to test this connection.

Of the targets displaying H_2 emission with extended blue wings, DF Tau, DK Tau, HN Tau, IP Tau, RECX-15, and RW Aur also have reasonably high S/N [0,1] progression emission lines in their spectra. The [0,1] linewidths are statistically narrower than those from [1,7] and [1,4], also suggesting that outflow contributions to the [1,4] and [1,7] progressions are present in these targets (Walter et al. 2003). RW Aur shows the strongest outflow emission in the survey, with both red- and blue-shifted emission observed. It is not clear that there is a narrow disk H_2 component present in this source. We show a blow-up of bright lines from the [1,7] and [1,4] progressions in RW Aur in Figure 8. RW Aur is known to have a bipolar outflow, with the red component (v_{out} ∼ +100 km s^{-1}) being brighter and higher density than the blue (Hirth et al. 1994; Melnikov et al. 2009). Due to the COS aperture vignetting function, the observed spectra will be dominated by the inner ≈ 1″ of the RW Aur jet. Figure 8 shows that the H_2 emission peaks at an observed velocity 80 − 110 km s^{-1} to the red of the stellar velocity (+14 km s^{-1}; Hartmann et al. 1986), suggesting that the molecular emission arises in material that is approximately cospatial with the forbidden atomic line (e.g., [S II] λ6731 Å) emission (Woitas et al. 2002; Melnikov et al. 2009; Hartigan & Hillenbrand 2009). The near-IR H_2 outflow from RW Aur is centered near ∼ +44 km s^{-1} (Beck et al. 2008), significantly bluer than the peak of the far-UV H_2 velocity profile. It is not clear if this indicates a difference in the physical structure of the UV and IR-emitting H_2, or can be attributed to blending of low- and high-

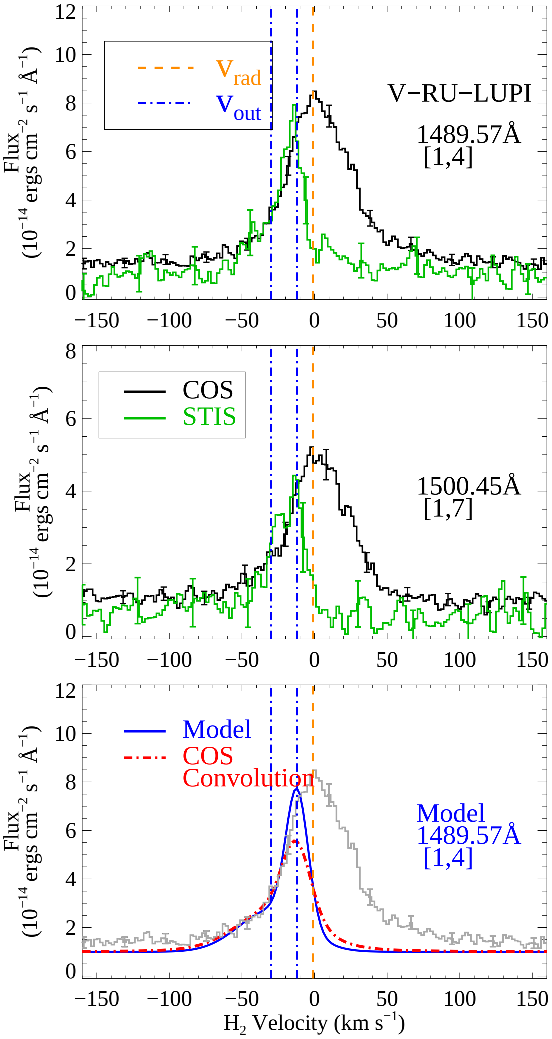

Fig. 9.— A comparison of archival STIS spectra of H_2 emission lines from RU Lupi (*green*) and new observations from COS (*black*). The stellar radial velocity is indicated with the orange dashed line and the outflow velocities from Herczeg et al. (2006) are shown as the dash-dotted blue lines. Strong lines from the [1,4] and [1,7] progressions are shown in the top two panels, and the bottom panel shows the two-component spectral fit for the STIS observations in blue (Herczeg et al. 2006). This profile, convolved with the 1490 Å COS LSF is shown as the red dash-dotted line and the observed COS data are shown in gray. The COS data are consistent with the stellar radial velocity and do not display asymmetric outflow profiles as strong as was observed by STIS. This difference may be due to a physical change in the inner regions of RU Lupi or could be explained by angular extension along the dispersion axis in the COS data (§4.2.1).

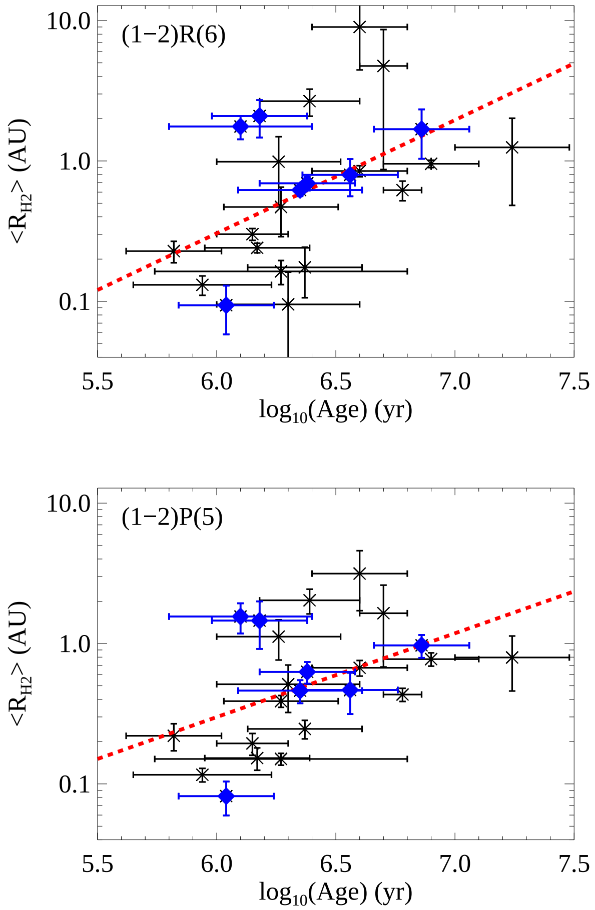

Fig. 10.— The time evolution of the average radial position of the H_2 emission in our sample, as defined by the Gaussian line-widths of the [1,7] (pumped through the (1 – 2) R(6) absorption line) and [1,4] (pumped through the (1 – 2) P(5) absorption line) progressions (see §3.2 for a discussion). Only targets with disk inclinations $i > 15°$ were considered. The red dashed line represents the empirical relation between the average radius of the H_2 emitting disk and the system age (Equation 3) for the [1,7] and [1,4] progressions. The two H_2 progressions show a similar behavior with system age. The Spearman rank correlation coefficient for increasing molecular radius with system age for both H_2 progressions is ≈ 0.52. The blue diamonds indicate targets with inclinations derived from sub-mm dust continua (Andrews & Williams 2007; Andrews et al. 2011).

velocity gas in the lower spectral resolution near-IR data. For the remaining targets, the blue-wings are relatively weak, typically only perturbations from the narrower, presumably disk-dominated H_2 velocity profiles. Further study using coadded spectra from several progressions would be useful for clarifying the outflow contribution and structure in these targets.

The observed H_2 velocity profiles of RU Lupi are puzzling. Using higher spectral resolution observations from STIS, Herczeg et al. (2005b, 2006) found that essentially all of the fluorescent H_2 was contained in two blue-shifted components, -12 and -30 km s^{-1} relative to the radial velocity of the star. While a blue-wing is apparent in the COS observations, the emission is well-fit by a single component at the radial velocity of the star. In Figure 9, we compare the COS observations (obtained in 2011 using the 2.5″ diameter Primary Science Aperture) with the STIS observations (obtained in 2000 using the 0.2″ × 0.06″ slit). The apparent line-center velocity shift is $\approx 15 - 20$ km s^{-1}, larger than the zero-point calibration of the COS wavelength solution[14]. Furthermore, the line-shape is fundamentally different in a way that cannot be explained by resolution differences between the two instruments. In the bottom panel of Figure 9, we reconstruct a model two-Gaussian profile (solid blue line) using the fit parameters from Herczeg et al. (2006). That profile, convolved with the COS LSF at 1490 Å (Kriss 2011), is displayed as the red dash-dotted curve. CTTSs (and in particular RU Lupi; Gahm et al. 2008) are known to be time-variable, therefore it is not surprising that the peak flux has changed, but the line center and emission line shapes are not consistent.

---

[14] Calibration of the COS wavelength solution is limited by systematic uncertainty in the far-UV detector geometric correction.

Herczeg et al. (2006) found that the H_2 fluorescence in RU Lupi was spatially extended, although the small size of the STIS aperture makes it difficult to predict the effects of spatial extension in the larger COS aperture. An aperture offset of $\gtrsim 0.4''$ would be required for significant reduction in the instrumental resolving power, but angular extension of the H_2 emitting region may be able to alter both the velocity centroid and the line-width. In the dispersion direction, if we attribute the entire 20 km s^{-1} offset to extended emission, this leads to a $0.2''$ displacement (at the 24.3 milliarcseconds pixel^{-1} dispersion-direction plate-scale of the G160M mode). We cannot constrain the angular extent of the RU Lupi H_2 lines in the dispersion direction, but we note that the optical forbidden line emission ([O I] and [S II]) are extended to $\sim 0.2''$ at a position angle of $\sim 225°$ (Takami et al. 2001). If the H_2 emission lines observed in the COS spectra are cospatial with the forbidden line emission, then this could produce the $\sim +$ 20 km s^{-1} velocity offset. Therefore, it is possible that spatial extension of the H_2 emitting gas along this axis could explain the differences in line shape between the STIS and COS observations. We compared the cross-dispersion profile of the two-dimensional spectrogram of the RU Lupi observations (over the range $\Delta\lambda \sim 1420 - 1450$ Å) with that of the DA white dwarf WD0320-539. The two spectra were centered to within 0.5 pixels ($\approx 0.05''$) in the cross-dispersion direction and had nearly identical profile FWHMs (4.5 pixels for WD0320, 4.8 pixels for RU Lupi).

We conclude therefore that either RU Lupi has spatial extent along the dispersion axis, or the spectral profile differences between the COS and STIS epochs are caused by a physical change in the system. RU Lupi may continue to be outflow dominated, however the COS observations raise the possibility that that RU Lupi was observed during an episode of strong outflow in 2000 or that the geometry has evolved such that disk-illumination by Lyα contributed more strongly during the 2011 observations. Continued spectral monitoring of these loopy line profiles would be interesting.

4.2.2. *H_2 Disks*

The high S/N H_2 lines in the majority of our sample targets can be adequately described by a single Gaussian emission component at the stellar radial velocity. Bearing in mind the added uncertainty introduced by blue-shifted H_2 in some targets, we conclude that most of the observed fluorescent emission originates in a disk. This is in contrast with the near-IR H_2 study of Beck et al. (2008); however, that study targeted stars known to have strong outflows, which is not the case with the sample presented here. Using the velocity-resolved H_2 line profiles, $\langle R_{H2} \rangle$ was calculated for the [1,7] and [1,4] progressions. The radial distributions as a function of system age are displayed in Figure 10. The general result is that the average location of the emitting H_2 gas in the inner disk moves outward from ~ 0.25 AU to ~ 2 AU as the system evolves from $1 - 10$ Myr.

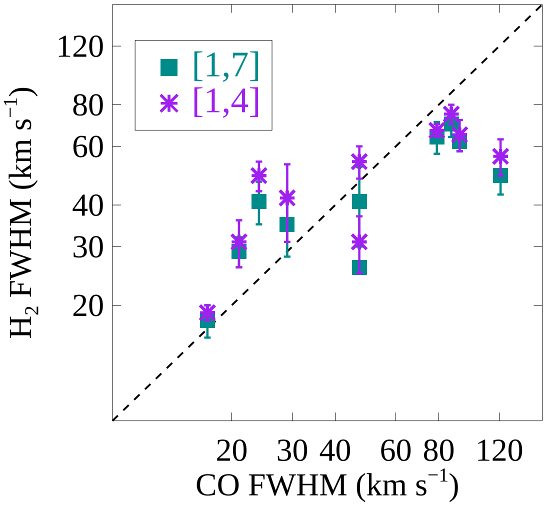

FIG. 11.— A comparison of the emission line FWHMs of H_2 (this work) and CO (Salyk et al. 2011a; Bast et al. 2011). The squares are the Gaussian line-widths of the [1,7] progression and the stars are the Gaussian line-widths of the [1,4] progression. The dashed line represents the expected correlation if the H_2 and CO line-widths are the same.

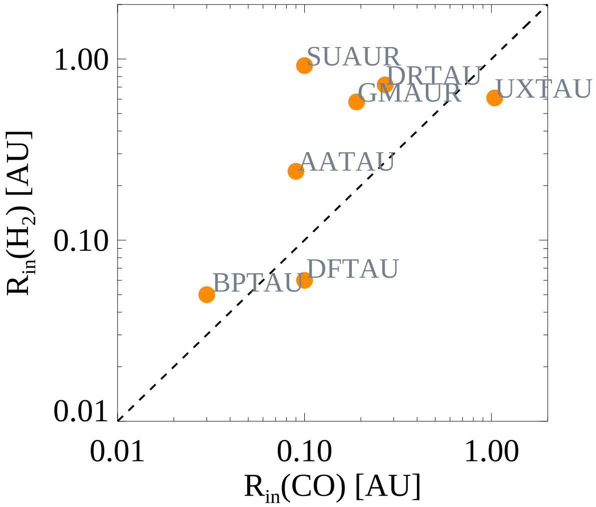

FIG. 12.— A comparison of inner radii (R_{in}) of the molecular disk traced by H_2 (this work) and CO (Salyk et al. 2011a). The dashed line represents the expected correlation if the H_2 and CO emission are co-spatial. R_{in} is defined as the Keplerian radius corresponding to an orbital velocity of 1.7 × HWHM of the Gaussian line fits (§3.2). R_{in}(H_2) is computed from the [1,7] progression for this comparison. Except in the case of SU Aur, R_{in}(H_2) and R_{in}(CO) are the same to within a factor of three, suggesting that the observed CO and H_2 orbit at similar radii.

The relationship between the system age and the average H_2 radius can be characterized by the simple empirical formula

$$log_{10}\langle R(H_2)\rangle_{[1,7]} = 0.81 \; log_{10}(Age) - 5.36 \tag{3}$$

where $\langle R_{H2} \rangle_{[1,7]}$ is in AU and the age is in years. The coefficients in Equation 3 [-5.36 ± 1.91, 0.81 ± 0.30] are computed from a χ^2 minimization of a linear function of $\log_{10}$(Age) and $\log_{10}\langle R_{H2}\rangle_{[1,7]}$. The Spearman rank correlation coefficient for increasing molecular radius with system age is 0.52 with a deviation from zero of 1.1×10^{-2}, meaning that there is a relatively low probability that $\log_{10}$(Age) and $\log_{10}\langle R_{H2}\rangle_{[1,7]}$ are uncorrelated. Targets with disk inclinations derived from submm dust continuum observations (Andrews & Williams 2007; Andrews et al. 2011) are plotted as the blue diamonds in Figure 10. There is a large spread in the distribution of $\langle R_{H2}\rangle$ with age. We suggest that in addition to contamination by outflows, uncertainties in the stellar mass, inclination angle, and stellar age all contribute to the dispersion in this correlation. With the exception of CS Cha (§4.3), the H_2 in all disks is concentrated at $a \lesssim 3$ AU.

The weak trend towards larger radii as a function of age suggests a scenario where the average molecular emission radius moves to beyond ≈ 1 AU in about 10 Myr. It is not immediately clear how to interpret this result, and we remind the reader of the ingredients necessary to produce H_2 fluorescence in a disk. The H_2 opacity must be high enough to absorb a significant number of Lyα photons, requiring both appreciable column densities and a sufficient population of H_2 in excited ro-vibrational states. The latter requires a hot ($T(H_2) \gtrsim 2000$ K) molecular layer, possibly with a contribution by intense illumination from the $\lambda \leq 1120$ Å continuum from the central star + accretion shocks (Nomura et al. 2007; France et al. 2012). The second major requirement for observable fluorescence is a geometry where the disk subtends a substantial angular cross-section of the Lyα emitting area, that is, the disk must be sufficiently flared in order to intercept enough Lyα photons to excite the observed emission. The observation of larger H_2 radii as a function of time suggests that one or more of these criteria are not being met in the inner ≈ 1 AU in the more evolved systems. It may be that the hot H_2 is in the process of dissipating from this region, possibly due to dynamical clearing by a protoplanet, enhanced H_2 dissociation as this region is less shielded by grains, or photoevaporation by energetic radiation from the central star. Alternatively, this result may indicate that the flaring angle in the inner disk is decreasing across our sample, suggesting an evolution of the vertical structure of the disk on timescales of a few Myr. Improved stellar masses and ages, and larger samples of well-determined disk inclinations would allow better characterization of the relation (or lack thereof) between molecular radius and age, enabling a better understanding of the evolution of inner gas disks.

4.2.3. *Comparison with near-IR H_2 Emission*

Quadrupole rovibrational line emission from H_2 (most notably the (1 – 0) S(1) $\lambda 2.1$ μm line) has been detected around several CTTSs (Bary et al. 2003; Itoh et al. 2003; Carmona et al. 2007; Bary et al. 2008). While the number of objects available for direct comparison is small, it seems that the Lyα-pumped H_2 emission arises interior to the near-IR emission lines (although see §4.3 for the case of the transitional disk CS Cha). Typical emission line widths for the near-IR H_2 sample presented in Bary et al. (2008) are FWHM ≤ 20 km s^{-1}, and are thought to originate at radial distances of a few to a few tens of AU. Similarly, Bary et al. (2003) observed (1 – 0) S(1) emission in LkCa15 with FWHM ≤ 14 km s^{-1} and suggested that the emitting gas was located between 10 – 30 AU from the star. This is a factor of ≈ 4 narrower than the FWHM$_{[1,7]} = 53 \pm 3$ km s^{-1} that we observe in the LkCa15 UV spectrum.

RECX-15 is the only disk in the η Cha region to emit a measurable flux of H_2 in the (1 – 0) S(1) line (Ramsay Howat & Greaves 2007). The near-IR H_2 line widths (18 ± 1.2 km s^{-1}) are a factor of ≈ 2.3 smaller than measured in the COS spectra of RECX-15 (41 ± 4 km s^{-1}), although we note that outflows do contribute to the RECX-15 ultraviolet H_2 spectra. The near-IR H_2 emission from disks is typically interpreted as disk surface gas excited by energetic radiation. Including the effects of grain grown, UV, and X-ray illumination, Nomura et al. (2007) have demonstrated that gas temperatures in the range 1500 – 3000 K can be maintained in the disk surface to radial distances of ≈ 10 AU from the central star, therefore the excitation conditions necessary to both produce near-IR emission and to enable Lyα-pumping appear to exist to at least this radius. However, the fluorescent ultraviolet emission is dominated by H_2 nearest to the source of Lyα photons.

4.2.4. *Comparison with CO Emission*

Comparing the line-widths of different molecular species can provide an observational constraint on the composition and physical structure of inner gas disks. Spectral observations of the 4.7 μm fundamental band CO emission are a widely used tracer for this material (Salyk et al. 2008, 2009), and understanding the molecular structure and the degree to which various spectral diagnostics trace the same gas are useful towards a more complete picture of the planet-forming regions around CTTSs. Figure 11 shows a comparison of the Gaussian FWHMs of CO and H_2 for the subsample of our targets that have been observed by high-resolution mid-IR spectrographs (Salyk et al. 2011a; Bast et al. 2011). The emission line-widths from the [1,7] and [1,4] H_2 progressions are self-consistent in all cases and approximately equal the CO line-widths up to FWHM ≈ 60 km s^{-1}. At larger CO line-widths, the H_2 FWHMs do not exceed 70 – 80 km s^{-1}, which may indicate a physical boundary condition inside of which H_2 is subject to collisional and/or photodissociation.

The inner radii of the H_2 and CO disks can also be directly compared. The calculated H_2 inner radii are presented in Table 3, and Figure 12 compares the ultraviolet H_2 (UV-H_2) and infrared CO (IR-CO) radii (Salyk et al. 2011a); the dashed horizontal line represents a one-to-one relation. With one exception, $R_{in}(H_2)$ and R_{in}(CO) are the same to within a factor of three. The agreement between the two molecules is rather remarkable given that we are comparing different species, excited by different mechanisms (photo-excitation vs. collisional excitation), observed at different epochs in different wavebands. The notable exception is SU Aur, whose $R_{in}(H_2)$ is approximately an order magnitude larger than its corresponding R_{in}(CO), possibly due to H_2 emission from nebulosity associated with this star. The agreement between the

IR-CO emission and the UV-H_2 emission is also interesting in light of the recent discovery of large amounts of CO emission in the UV spectra of CTTSs (UV-CO; France et al. 2011b). Schindhelm et al. (2012a) present an initial survey of this emission, showing that the line-widths of UV-CO are systematically narrower than those of UV-H_2. Their interpretation favors a picture where the UV-CO originates in a cooler molecular layer (T_{rot}(CO) $\sim$ 500 K) at larger semi-major axes ($a \gtrsim 2$ AU) than both the UV-H_2 and the IR-CO, consistent with the results presented here.

4.3. *H_2 in Transitional Disks*

The majority of H_2 emission in the targets in our sample originates from $a \lesssim 3$ AU. A notable outlier from the average H_2 radii presented in Table 3 is CS Cha, which lies at significantly larger $\langle R_{H2} \rangle_{[1,7]}$ than the rest of the disks studied here. The [1,7] line-width of CS Cha is 18 ± 7 km s^{-1}, which makes it the only unresolved moderate inclination target[15], and allows us to place a lower limit on the average H_2 emission radius, $\langle R_{H2} \rangle_{[1,7]} \geq 9$ AU. CS Cha is a transitional disk, showing the largest mid-IR spectral slope in our sample, n_{13-31} = 2.89 (Furlan et al. 2009; see Table 3). Modeling of the *Spitzer*-IRS mid-IR spectrum of CS Cha reveals a truncation of the inner disk dust distribution at $a \approx 43$ AU (Espaillat et al. 2007b), possibly the result of a dynamical interaction with a companion star (Guenther et al. 2007, but see also Espaillat et al. 2011). The new *HST* data presented here confirms the presence of molecular gas in the system (Bary et al. 2008), and while we cannot rule out the possibility that this gas is co-spatial with the dust at $a \gtrsim 40$ AU, this would imply that hot molecular gas ($T(H_2) \geq 2000$ K) exists at large radial distances from the star. Therefore, because only ($N(H_2) \gtrsim 10^{18}$ cm^{-2}) is required to produce detectable fluorescence, this emission may originate in the tenuous molecular material in the disk gap, or if Lyα photons can propagate through the gap, this emission may arise from the edge of the directly exposed wall at $\sim$ 43 AU.

The H_2 emitting material we observe in CS Cha may be physically associated with the [Ne II] emission observed by Espaillat et al. (2007b), but that cannot be conclusively determined from the available observations. We can rule out an origin in the optically thin dust disk inside of 1 AU, as our limit on the H_2 inner disk radius in CS Cha is $R_{in}(H_2) \geq 3$ AU.

CS Cha is one example of a generic property of our sample: H_2 is common in the inner regions of accreting transitional disks ($n_{13-31} > 0.5$). In addition to CS Cha, our sample includes the well-studied transitional systems DM Tau, GM Aur, UX Tau A, LkCa15, HD 135344B and TW Hya (Calvet et al. 2005, 2002; Espaillat et al. 2007c). H_2 emission is found to originate inside the dust hole in these systems, $\langle R_{H2} \rangle < R_{dust}$, consistent with the origin of the IR-CO gas in the inner regions of transitional disks (Salyk et al. 2009, 2011a) and previous observations of near-IR rovibrational emission from H_2 (Bary et al. 2008).

5. SUMMARY

We have presented the most sensitive survey of H_2 in protoplanetary environments to date. The majority of this work was made possible by the combination of large effective area and low instrumental background at moderate spectral resolution provided by the *HST*-Cosmic Origins Spectrograph. We have used this survey to measure the time evolution of both the spatial distribution and the luminosity of H_2 in young, low-mass disks for the first time. Below we summarize the primary results of this work:

1. We obtained far-UV spectra of 34 T Tauri stars: 27 accreting CTTSs and 7 non-accreting WTTSs. Of these, 100% of the accreting sources display a measureable amount of H_2 emission, providing direct evidence for the interaction of a strong Lyα radiation field with the molecular disk surface.

2. We found that the H_2 luminosity is well correlated with the Lyα and C IV luminosity, consistent with a scenario where gas-rich disks fuel larger accretion rates that produce energetic radiation.

3. The H_2 luminosity is observed to decline with age, although H_2-rich systems persist to ages $\sim$ 10 Myr.

4. We measured resolved H_2 line profiles of 23 targets with inclination angles > 15° and found that these line profiles are reasonably well fit by a single Gaussian component at or near the stellar radial velocity. Assuming a disk origin for these targets, we used the line-widths to constrain the spatial distribution of the emitting molecules to $a \lesssim 3$ AU in most cases.

5. The inner radii of H_2 disks are roughly consistent with those of CO disks (measured from $\lambda \sim 5$ μm spectroscopy).

6. Strong H_2 emission is observed at $a \gtrsim 0.2$ AU in a subsample of transitional disks ($n_{13-31} > 0.5$).

We thank Tom Ayres for custom processing of the STIS observations and the DAO of Tau team for enjoyable discussions during the course of this work. KF thanks Phil Armitage for helpful discussion regarding gas giant migration. We acknowledge the technical efforts of Nico Nell and David Morris, and ES and KF thank Brian Wood for input on Lyα profile reconstruction. RDA acknowledges support from the Science & Technology Facilities Council (STFC) through an Advanced Fellowship (ST/G00711X/1). This work was supported by NASA grants NNX08AC146 and NAS5-98043 to the University of Colorado at Boulder (*HST* programs 11533 and 12036) and made use of data from *HST* GO programs 8041, 11616, 11828, and 12361.

REFERENCES

---

[15] The [1,4] line-width is 29 ± 12 km s^{-1}, consistent with the [1,7] result. Bary et al. (2008) report a near-IR line-width of 12.6 km s^{-1}, which would be unresolved in our COS observations.

Akeson, R. L., Ciardi, D. R., van Belle, G. T., & Creech-Eakman, M. J. 2002, ApJ, 566, 1124
Alencar, S. H. P., Melo, C. H. F., Dullemond, C. P., Andersen, J., Batalha, C., Vaz, L. P. R., & Mathieu, R. D. 2003, A&A, 409, 1037
Alexander, R. D., Clarke, C. J., & Pringle, J. E. 2006, MNRAS, 369, 229
Andrews, S. M. & Williams, J. P. 2007, ApJ, 659, 705
Andrews, S. M., Wilner, D. J., Espaillat, C., Hughes, A. M., Dullemond, C. P., McClure, M. K., Qi, C., & Brown, J. M. 2011, ApJ, 732, 42
Ardila, D. R., Basri, G., Walter, F. M., Valenti, J. A., & Johns-Krull, C. M. 2002, ApJ, 566, 1100
Armitage, P. J. 2007, ApJ, 665, 1381
Armitage, P. J., Clarke, C. J., & Palla, F. 2003, MNRAS, 342, 1139
Armitage, P. J., Livio, M., Lubow, S. H., & Pringle, J. E. 2002, MNRAS, 334, 248
Ayres, T. R. 2010, ApJS, 187, 149
Bary, J. S., Weintraub, D. A., & Kastner, J. H. 2003, ApJ, 586, 1136
Bary, J. S., Weintraub, D. A., Shukla, S. J., Leisenring, J. M., & Kastner, J. H. 2008, ApJ, 678, 1088
Bast, J., Brown, J., Herczeg, G., van Dishoek, E., & Pontoppidan, K. 2011, A&A, 1, 0
Beck, T. L., McGregor, P. J., Takami, M., & Pyo, T.-S. 2008, ApJ, 676, 472
Bertout, C., Siess, L., & Cabrit, S. 2007, A&A, 473, L21
Bethell, T. J. & Bergin, E. A. 2011, ApJ, 739, 78
Brittain, S. D., Najita, J. R., & Carr, J. S. 2009, ApJ, 702, 85
Calvet, N., D'Alessio, P., Hartmann, L., Wilner, D., Walsh, A., & Sitko, M. 2002, ApJ, 568, 1008
Calvet, N., D'Alessio, P., Watson, D. M., Franco-Hernández, R., Furlan, E., Green, J., Sutter, P. M., Forrest, W. J., Hartmann, L., Uchida, K. I., Keller, L. D., Sargent, B., Najita, J., Herter, T. L., Barry, D. J., & Hall, P. 2005, ApJ, 630, L185
Calvet, N. & Gullbring, E. 1998, ApJ, 509, 802
Carmona, A., van den Ancker, M. E., Henning, T., Goto, M., Fedele, D., & Stecklum, B. 2007, A&A, 476, 853
Carmona, A., van den Ancker, M. E., Henning, T., Pavlyuchenkov, Y., Dullemond, C. P., Goto, M., Thi, W. F., Bouwman, J., & Waters, L. B. F. M. 2008, A&A, 477, 839
Carr, J. S. & Najita, J. R. 2008, Science, 319, 1504
—. 2011, ApJ, 733, 102
Chiang, E. & Murray-Clay, R. 2007, Nature Physics, 3, 604
Coffey, D., Bacciotti, F., Woitas, J., Ray, T. P., & Eislöffel, J. 2004, ApJ, 604, 758
Comerón, F. & Fernández, M. 2010, A&A, 511, A10+
Comerón, F., Fernández, M., Baraffe, I., Neuhäuser, R., & Kaas, A. A. 2003a, A&A, 406, 1001
—. 2003b, A&A, 406, 1001
Danforth, C. W., Keeney, B. A., Stocke, J. T., Shull, J. M., & Yao, Y. 2010, ApJ, 720, 976
Dodson-Robinson, S. E. & Salyk, C. 2011, ApJ, 738, 131
Eisner, J. A., Hillenbrand, L. A., White, R. J., Bloom, J. S., Akeson, R. L., & Blake, C. H. 2007, ApJ, 669, 1072
Elias, J. H. 1978, ApJ, 224, 857
Espaillat, C., Calvet, N., D'Alessio, P., Bergin, E., Hartmann, L., Watson, D., Furlan, E., Najita, J., Forrest, W., McClure, M., Sargent, B., Bohac, C., & Harrold, S. T. 2007a, ApJ, 664, L111
—. 2007b, ApJ, 664, L111
Espaillat, C., Calvet, N., D'Alessio, P., Hernández, J., Qi, C., Hartmann, L., Furlan, E., & Watson, D. M. 2007c, ApJ, 670, L135
Espaillat, C., D'Alessio, P., Hernández, J., Nagel, E., Luhman, K. L., Watson, D. M., Calvet, N., Muzerolle, J., & McClure, M. 2010, ApJ, 717, 441
Espaillat, C., Furlan, E., D'Alessio, P., Sargent, B., Nagel, E., Calvet, N., Watson, D. M., & Muzerolle, J. 2011, ApJ, 728, 49
Evans, II, N. J., Dunham, M. M., Jørgensen, J. K., Enoch, M. L., Merín, B., van Dishoeck, E. F., Alcalá, J. M., Myers, P. C., Stapelfeldt, K. R., Huard, T. L., Allen, L. E., Harvey, P. M., van Kempen, T., Blake, G. A., Koerner, D. W., Mundy, L. G., Padgett, D. L., & Sargent, A. I. 2009, ApJS, 181, 321
Fang, M., van Boekel, R., Wang, W., Carmona, A., Sicilia-Aguilar, A., & Henning, T. 2009, A&A, 504, 461
Fedele, D., van den Ancker, M. E., Henning, T., Jayawardhana, R., & Oliveira, J. M. 2010, A&A, 510, A72
Feigelson, E. D., Lawson, W. A., & Garmire, G. P. 2003a, ApJ, 599, 1207
—. 2003b, ApJ, 599, 1207
Fogel, J. K. J., Bethell, T. J., Bergin, E. A., Calvet, N., & Semenov, D. 2011, ApJ, 726, 29
France, K., Burgh, E. B., Herczeg, G. J., Schindhelm, E., Yang, H., Abgrall, H., Roueff, E., Brown, A., Brown, J. M., & Linsky, J. L. 2012, ApJ, 744, 22
France, K., Linsky, J. L., Brown, A., Froning, C. S., & Béland, S. 2010, ApJ, 715, 596
France, K., Schindhelm, E., Burgh, E. B., Herczeg, G. J., Harper, G. M., Brown, A., Green, J. C., Linsky, J. L., Yang, H., Abgrall, H., Ardila, D. R., Bergin, E., Bethell, T., Brown, J. M., Calvet, N., Espaillat, C., Gregory, S. G., Hillenbrand, L. A., Hussain, G., Ingleby, L., Johns-Krull, C. M., Roueff, E., Valenti, J. A., & Walter, F. M. 2011a, ApJ, 734, 31
France, K., Yang, H., & Linsky, J. L. 2011b, ApJ, 729, 7
Furlan, E., Hartmann, L., Calvet, N., D'Alessio, P., Franco-Hernández, R., Forrest, W. J., Watson, D. M., Uchida, K. I., Sargent, B., Green, J. D., Keller, L. D., & Herter, T. L. 2006, ApJS, 165, 568
Furlan, E., Watson, D. M., McClure, M. K., Manoj, P., Espaillat, C., D'Alessio, P., Calvet, N., Kim, K. H., Sargent, B. A., Forrest, W. J., & Hartmann, L. 2009, ApJ, 703, 1964
Gahm, G. F., Walter, F. M., Stempels, H. C., Petrov, P. P., & Herczeg, G. J. 2008, A&A, 482, L35
Garcia Lopez, R., Natta, A., Testi, L., & Habart, E. 2006, A&A, 459, 837
Gómez de Castro, A. I. 2009, ApJ, 698, L108
Gorti, U., Dullemond, C. P., & Hollenbach, D. 2009, ApJ, 705, 1237
Grady, C. A., Woodgate, B., Torres, C. A. O., Henning, T., Apai, D., Rodmann, J., Wang, H., Stecklum, B., Linz, H., Williger, G. M., Brown, A., Wilkinson, E., Harper, G. M., Herczeg, G. J., Danks, A., Vieira, G. L., Malumuth, E., Collins, N. R., & Hill, R. S. 2004, ApJ, 608, 809
Green, J. C., Froning, C. S., Osterman, S., Ebbets, D., Heap, S. H., Linsky, C. L. J. L., Savage, B. D., Sembach, K., Shull, J. M., Siegmund, O. H. W., Snow, T. P., Spencer, J., Stern, S. A., Stocke, J., Welsh, B., Beland, S., Burgh, E. B., Danforth, C., France, K., Keeney, B., McPhate, J., Penton, S. V., Andrews, J., Brownsberger, K., Morse, J., & Wilkinson, E. 2011, ArXiv e-prints
Guenther, E. W., Esposito, M., Mundt, R., Covino, E., Alcalá, J. M., Cusano, F., & Stecklum, B. 2007, A&A, 467, 1147
Gullbring, E., Calvet, N., Muzerolle, J., & Hartmann, L. 2000, ApJ, 544, 927
Gullbring, E., Hartmann, L., Briceno, C., & Calvet, N. 1998, ApJ, 492, 323
Günther, H. M. & Schmitt, J. H. M. M. 2008, A&A, 481, 735
Haisch, Jr., K. E., Lada, E. A., & Lada, C. J. 2001, ApJ, 553, L153
Hartigan, P. & Hillenbrand, L. 2009, ApJ, 705, 1388
Hartmann, L., Calvet, N., Gullbring, E., & D'Alessio, P. 1998, ApJ, 495, 385
Hartmann, L., Hewett, R., Stahler, S., & Mathieu, R. D. 1986, ApJ, 309, 275
Hayashi, C., Nakazawa, K., & Nakagawa, Y. 1985, in Protostars and planets II (A86-12626 03-90). Tucson, AZ, University of Arizona Press, 1985, p. 1100-1153., ed. D. C. Black & M. S. Matthews, 1100–1153
Herczeg, G. J. & Hillenbrand, L. A. 2008, ApJ, 681, 594
Herczeg, G. J., Linsky, J. L., Valenti, J. A., Johns-Krull, C. M., & Wood, B. E. 2002, ApJ, 572, 310
Herczeg, G. J., Linsky, J. L., Walter, F. M., Gahm, G. F., & Johns-Krull, C. M. 2006, ApJS, 165, 256
Herczeg, G. J., Najita, J. R., Hillenbrand, L. A., & Pascucci, I. 2007, ApJ, 670, 509
Herczeg, G. J., Walter, F. M., Linsky, J. L., Gahm, G. F., Ardila, D. R., Brown, A., Johns-Krull, C. M., Simon, M., & Valenti, J. A. 2005a, AJ, 129, 2777
—. 2005b, AJ, 129, 2777

Herczeg, G. J., Wood, B. E., Linsky, J. L., Valenti, J. A., & Johns-Krull, C. M. 2004, ApJ, 607, 369

Hernández, J., Hartmann, L., Megeath, T., Gutermuth, R., Muzerolle, J., Calvet, N., Vivas, A. K., Briceño, C., Allen, L., Stauffer, J., Young, E., & Fazio, G. 2007, ApJ, 662, 1067

Hirth, G. A., Mundt, R., Solf, J., & Ray, T. P. 1994, ApJ, 427, L99

Hussain, G. A. J., Collier Cameron, A., Jardine, M. M., Dunstone, N., Ramirez Velez, J., Stempels, H. C., Donati, J.-F., Semel, M., Aulanier, G., Harries, T., Bouvier, J., Dougados, C., Ferreira, J., Carter, B. D., & Lawson, W. A. 2009, MNRAS, 398, 189

Ida, S. & Lin, D. N. C. 2004, ApJ, 604, 388

Ingleby, L., Calvet, N., Bergin, E., Herczeg, G., Brown, A., Alexander, R., Edwards, S., Espaillat, C., France, K., Gregory, S. G., Hillenbrand, L., Roueff, E., Valenti, J., Walter, F., Johns-Krull, C., Brown, J., Linsky, J., McClure, M., Ardila, D., Abgrall, H., Bethell, T., Hussain, G., & Yang, H. 2011a, ArXiv e-prints

Ingleby, L., Calvet, N., Bergin, E., Yerasi, A., Espaillat, C., Herczeg, G., Roueff, E., Abgrall, H., Hernández, J., Briceño, C., Pascucci, I., Miller, J., Fogel, J., Hartmann, L., Meyer, M., Carpenter, J., Crockett, N., & McClure, M. 2009, ApJ, 703, L137

Ingleby, L., Calvet, N., Hernández, J., Briceño, C., Espaillat, C., Miller, J., Bergin, E., & Hartmann, L. 2011b, AJ, 141, 127

Itoh, Y., Sugitani, K., Ogura, K., & Tamura, M. 2003, PASJ, 55, L77

Jensen, E. L. N. & Mathieu, R. D. 1997, AJ, 114, 301

Johns-Krull, C. M. & Valenti, J. A. 2001, ApJ, 561, 1060

Johns-Krull, C. M., Valenti, J. A., & Linsky, J. L. 2000, ApJ, 539, 815

Kenyon, S. J. & Hartmann, L. 1995, ApJS, 101, 117

Kim, K. H., Watson, D. M., Manoj, P., Furlan, E., Najita, J., Forrest, W. J., Sargent, B., Espaillat, C., Calvet, N., Luhman, K. L., McClure, M. K., Green, J. D., & Harrold, S. T. 2009, ApJ, 700, 1017

Kraus, A. L. & Hillenbrand, L. A. 2009, ApJ, 704, 531

Kraus, A. L., Ireland, M. J., Hillenbrand, L. A., & Martinache, F. 2012, ApJ, 745, 19

Kriss, G. A. 2011, Improved Medium Resolution Line Spread Functions for COS FUV Spectra, Tech. rep.

Lawson, W. A., Crause, L. A., Mamajek, E. E., & Feigelson, E. D. 2001, MNRAS, 321, 57

Lawson, W. A., Feigelson, E. D., & Huenemoerder, D. P. 1996, MNRAS, 280, 1071

Lawson, W. A., Lyo, A., & Muzerolle, J. 2004, MNRAS, 351, L39

Lepp, S. & Shull, J. M. 1983, ApJ, 270, 578

Luhman, K. L. 2004, ApJ, 602, 816

Luhman, K. L., Allen, P. R., Espaillat, C., Hartmann, L., & Calvet, N. 2010, ApJS, 186, 111

Mamajek, E. E., Lawson, W. A., & Feigelson, E. D. 1999, ApJ, 516, L77

Markwardt, C. B. 2009, in Astronomical Society of the Pacific Conference Series, Vol. 411, Astronomical Data Analysis Software and Systems XVIII, ed. D. A. Bohlender, D. Durand, & P. Dowler, 251

Melnikov, S. Y., Eislöffel, J., Bacciotti, F., Woitas, J., & Ray, T. P. 2009, A&A, 506, 763

Merín, B., Brown, J. M., Oliveira, I., Herczeg, G. J., van Dishoeck, E. F., Bottinelli, S., Evans, II, N. J., Cieza, L., Spezzi, L., Alcalá, J. M., Harvey, P. M., Blake, G. A., Bayo, A., Geers, V. G., Lahuis, F., Prusti, T., Augereau, J.-C., Olofsson, J., Walter, F. M., & Chiu, K. 2010, ApJ, 718, 1200

Muzerolle, J., Calvet, N., Hartmann, L., & D'Alessio, P. 2003, ApJ, 597, L149

Najita, J., Carr, J. S., & Mathieu, R. D. 2003, ApJ, 589, 931

Najita, J. R., Crockett, N., & Carr, J. S. 2008, ApJ, 687, 1168

Najita, J. R., Doppmann, G. W., Bitner, M. A., Richter, M. J., Lacy, J. H., Jaffe, D. T., Carr, J. S., Meijerink, R., Blake, G. A., Herczeg, G. J., & Glassgold, A. E. 2009, ApJ, 697, 957

Najita, J. R., Strom, S. E., & Muzerolle, J. 2007, MNRAS, 378, 369

Neuhäuser, R., Brandner, W., Eckart, A., Guenther, E., Alves, J., Ott, T., Huélamo, N., & Fernández, M. 2000, A&A, 354, L9

Nomura, H., Aikawa, Y., Tsujimoto, M., Nakagawa, Y., & Millar, T. J. 2007, ApJ, 661, 334

Osterman, S., Green, J., Froning, C., Béland, S., Burgh, E., France, K., Penton, S., Delker, T., Ebbets, D., Sahnow, D., Bacinski, J., Kimble, R., Andrews, J., Wilkinson, E., McPhate, J., Siegmund, O., Ake, T., Aloisi, A., Biagetti, C., Diaz, R., Dixon, W., Friedman, S., Ghavamian, P., Goudfrooij, P., Hartig, G., Keyes, C., Lennon, D., Massa, D., Niemi, S., Oliveira, C., Osten, R., Proffitt, C., Smith, T., & Soderblom, D. 2011, Ap&SS, 306

Pascucci, I., Gorti, U., Hollenbach, D., Najita, J., Meyer, M. R., Carpenter, J. M., Hillenbrand, L. A., Herczeg, G. J., Padgett, D. L., Mamajek, E. E., Silverstone, M. D., Schlingman, W. M., Kim, J. S., Stobie, E. B., Bouwman, J., Wolf, S., Rodmann, J., Hines, D. C., Lunine, J., & Malhotra, R. 2006, ApJ, 651, 1177

Pascucci, I., Hollenbach, D., Najita, J., Muzerolle, J., Gorti, U., Herczeg, G. J., Hillenbrand, L. A., Kim, J. S., Carpenter, J. M., Meyer, M. R., Mamajek, E. E., & Bouwman, J. 2007, ApJ, 663, 383

Pascucci, I., Sterzik, M., Alexander, R. D., Alencar, S. H. P., Gorti, U., Hollenbach, D., Owen, J., Ercolano, B., & Edwards, S. 2011, ApJ, 736, 13

Plavchan, P., Werner, M. W., Chen, C. H., Stapelfeldt, K. R., Su, K. Y. L., Stauffer, J. R., & Song, I. 2009, ApJ, 698, 1068

Pontoppidan, K. M., Blake, G. A., & Smette, A. 2011, ApJ, 733, 84

Pontoppidan, K. M., Blake, G. A., van Dishoeck, E. F., Smette, A., Ireland, M. J., & Brown, J. 2008a, ApJ, 684, 1323

—. 2008b, ApJ, 684, 1323

Quast, G. R., Torres, C. A. O., de La Reza, R., da Silva, L., & Mayor, M. 2000a, in IAU Symposium, Vol. 200, IAU Symposium, 28P–+

Quast, G. R., Torres, C. A. O., de La Reza, R., da Silva, L., & Mayor, M. 2000b, in IAU Symposium, Vol. 200, IAU Symposium, 28P–+

Ramsay Howat, S. K. & Greaves, J. S. 2007, MNRAS, 379, 1658

Ricci, L., Testi, L., Natta, A., Neri, R., Cabrit, S., & Herczeg, G. J. 2010, A&A, 512, A15+

Rice, W. K. M., Wood, K., Armitage, P. J., Whitney, B. A., & Bjorkman, J. E. 2003, MNRAS, 342, 79

Rodriguez, D. R., Kastner, J. H., Wilner, D., & Qi, C. 2010, ApJ, 720, 1684

Sacco, G. G., Flaccomio, E., Pascucci, I., Lahuis, F., Ercolano, B., Kastner, J. H., Micela, G., Stelzer, B., & Sterzik, M. 2012, ApJ, 747, 142

Salyk, C., Blake, G. A., Boogert, A. C. A., & Brown, J. M. 2009, ApJ, 699, 330

—. 2011a, ArXiv e-prints

Salyk, C., Pontoppidan, K. M., Blake, G. A., Lahuis, F., van Dishoeck, E. F., & Evans, II, N. J. 2008, ApJ, 676, L49

Salyk, C., Pontoppidan, K. M., Blake, G. A., Najita, J. R., & Carr, J. S. 2011b, ApJ, 731, 130

Saucedo, J., Calvet, N., Hartmann, L., & Raymond, J. 2003, ApJ, 591, 275

Schindhelm, E., France, K., Burgh, E. B., Herczeg, G. J., Green, J. C., Brown, A., Brown, J. M., & Valenti, J. A. 2012a, ApJ, 746, 97

Schindhelm, E., France, K., Herczeg, G., & Bergin, E. 2012b, ApJ

Shull, J. M. 1978, ApJ, 224, 841

Sicilia-Aguilar, A., Henning, T., & Hartmann, L. W. 2010, ApJ, 710, 597

Siess, L., Dufour, E., & Forestini, M. 2000, A&A, 358, 593

Simon, M., Dutrey, A., & Guilloteau, S. 2000, ApJ, 545, 1034

Stempels, H. C., Gahm, G. F., & Petrov, P. P. 2007, A&A, 461, 253

Strom, K. M., Strom, S. E., Edwards, S., Cabrit, S., & Skrutskie, M. F. 1989, AJ, 97, 1451

Takami, M., Bailey, J., Gledhill, T. M., Chrysostomou, A., & Hough, J. H. 2001, MNRAS, 323, 177

Torres, R. M., Loinard, L., Mioduszewski, A. J., & Rodríguez, L. F. 2007, ApJ, 671, 1813

Trilling, D. E., Lunine, J. I., & Benz, W. 2002, A&A, 394, 241

Valenti, J. A., Johns-Krull, C. M., & Linsky, J. L. 2000, ApJS, 129, 399

van Boekel, R., Min, M., Waters, L. B. F. M., de Koter, A., Dominik, C., van den Ancker, M. E., & Bouwman, J. 2005, A&A, 437, 189

van Leeuwen, F. 2007, A&A, 474, 653

Walter, F. M., Herczeg, G., Brown, A., Ardila, D. R., Gahm, G. F., Johns-Krull, C. M., Lissauer, J. J., Simon, M., & Valenti, J. A. 2003, AJ, 126, 3076
Ward, W. R. 1997, Icarus, 126, 261
Webb, R. A., Zuckerman, B., Platais, I., Patience, J., White, R. J., Schwartz, M. J., & McCarthy, C. 1999, ApJ, 512, L63
White, R. J. & Ghez, A. M. 2001, ApJ, 556, 265
Williams, J. P. & Cieza, L. A. 2011, ARA&A, 49, 67
Woitas, J., Ray, T. P., Bacciotti, F., Davis, C. J., & Eislöffel, J. 2002, ApJ, 580, 336
Wood, B. E. & Karovska, M. 2004, ApJ, 601, 502
Wood, B. E., Karovska, M., & Raymond, J. C. 2002, ApJ, 575, 1057
Wyatt, M. C. 2008, ARA&A, 46, 339
Yang, H., Herczeg, G. J., Linsky, J. L., Brown, A., Johns-Krull, C. M., Ingleby, L., Calvet, N., Bergin, E., & Valenti, J. A. 2012, ApJ, 744, 121
Yang, H., Linsky, J., & France, K. 2011, ApJ, 0, L1+